Parameter Influence on the Porous Bleed Performance with & without Shock-Boundary Layer Interaction

Julian Giehler*, Pierre Grenson†, and Reynald Bur‡
DAAA, ONERA, Université Paris Saclay, 92190 Meudon, France

Porous bleed systems are a common technique to control shock-boundary layer interactions and/or supersonic boundary layer. However, the influence of various design parameters is still unknown. Even though bleed models are required to minimize the costs of the design process, they often do not include parameter effects. In the present study, the effect of the hole diameter, the porosity level, and the length-to-diameter ratio are investigated by means of three-dimensional RANS simulations. The findings show an influence of the hole diameter on both flow control and efficiency of the porous bleed. A significant impact of the porosity level on the effective control of the shock-boundary layer interaction is found. In contrast, the length-to-diameter ratio does not influence the effective control but affects the efficiency of the system.

I. Nomenclature

Latin symbols

A	=	Area
A_p	=	Plate area
$A_{pl,ex}$	=	Plenum exit throat area
D	=	Hole diameter
H	=	Boundary layer shape factor
L	=	Hole length
M	=	Mach number
$\dot{m}$	=	Mass flow rate
p	=	Static pressure
$Q_{sonic,w}$	=	Surface sonic flow coefficient
R	=	Specific gas constant (air)
Re	=	Reynolds number
T	=	Static temperature
TR	=	Throat ratio
v	=	Transpiration velocity
x, y, z	=	Cartesian coordinates

Greek symbols

α	=	Angle of attack
δ ; δ_{99}	=	Boundary layer thickness
δ_1	=	Displacement thickness
δ_2	=	Momentum thickness
γ	=	Heat capacity ratio
ϕ	=	Porosity level
ρ	=	Density
τ	=	Shear stress

Subscripts

bl	=	Bleed condition
h	=	Hole condition
pl	=	Plenum condition
$sonic$	=	Sonic condition
t	=	Total condition
w	=	External wall conditions

II. Introduction

THE application of a porous bleed is a proven technology to mitigate the boundary layer separation caused by shock-boundary layer interactions in various applications such as supersonic air inlets. Typical bleed systems consist of a vast number of small holes which cover the area around or upstream of the shock foot. The principle is to remove the low-momentum air near the wall and, as a result, to generate a boundary layer profile that is less susceptible to separate for positive pressure gradients (see Fig. 1). Crucial for the system's success is a sufficient pressure ratio between the wall pressure and the pressure in the bleed plenum, which is located below the holes. Up to now, it remains challenging to predict the required pressure to remove the desired mass and also to estimate the effect of the bleed system on the boundary layer and, consequently, on the shock-boundary layer interaction.

*Ph.D. Student, Aerodynamics, Aeroelasticity, Acoustics Department, julian.giehler@onera.fr
†Research Scientist, Aerodynamics, Aeroelasticity, Acoustics Department, pierre.grenson@onera.fr
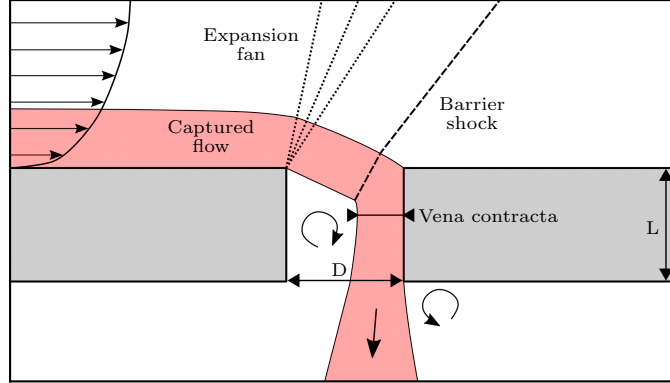‡Senior Research Scientist, Aerodynamics, Aeroelasticity, Acoustics Department, reynald.bur@onera.fr

Fig. 1 Schematic of the flow through a porous plate in supersonic flow

In the past, several researchers investigated the effect of porous bleed experimentally. In contrast to real applications, the porous bleed regions in experiments are scaled in size, and only a small number of rows [1–7], or even a single hole [8–10], is investigated. Moreover, the porous bleed is only globally regarded, which means that only little information about the flow in the individual holes exists [11, 12]. As a result, the longitudinal evolution of the local mass removal is unregarded, and all bleed holes are considered to work equally. Moreover, the knowledge about the influence of the bleed parameters (e.g., hole diameter, hole length-to-diameter ratio, porosity, etc.) is limited. Only a few studies focus on various plate geometries [2–4, 9, 10, 13].

In contrast to experiments, numerical investigations make extracting the mass flow rates for individual holes feasible. Nevertheless, recent numerical studies [7, 14–18] lack in showing and analyzing the local mass flow rates. Also, the change of the flow field in the holes along the porous bleed is unregarded. Similar to the experiments, the bleed region is observed globally without focusing on the interaction between the holes.

The lack of information about the local flow behavior complicates finding a suitable model that can capture the flow physics. Bleed models are unavoidable in the industrial context since the accurate meshing of all holes makes even Reynolds-Averaged Navier–Stokes (RANS) simulations very cost- and time-consuming. Bleed models can be applied as local boundary conditions without refining the mesh. Nevertheless, common bleed models [14, 19] also neglect the influence of bleed parameters and the hole's location. To the author's knowledge, only a few models consider bleed parameters or local porosity variations [4, 16, 20, 21]. More precise data are necessary to make clear statements about the working principle of bleed systems and create a more accurate bleed model valid for a large range of parameters.

In this investigation, a large dataset of bleed configurations is presented. The bleed parameters porosity, hole diameter, and hole length-to-diameter ratio are altered, and their influence on the removed mass flow rate, the boundary layer as well as on the shock-induced flow separation is illustrated. In contrast to previous studies, the mass flow rate is locally computed, allowing us to better understand the operation of a porous bleed.

The paper is organized as follows: In Sec. III, we introduce the physical domains to investigate the influence of the parameters. The numerical methodology is then explained in Sec. IV. Numerical results of the parametric study are presented in Sec. V for the supersonic boundary layer bleeding and in Sec. VI for the control of the shock-induced boundary layer separation.

III. Description of the problem

M	p_t	T_t	Re_x	Re_{δ_2}	δ_{99}	δ_1	δ_2	H
1.6	93 000 Pa	300 K	$12.7 \times 10^6/$m	5450	4.42 mm	0.58 mm	0.43 mm	1.35

Table 1 Physical properties of the investigated problems 5 mm upstream of the first bleed hole

A. Supersonic turbulent boundary layer bleeding

The first investigated problem is a supersonic flow on a flat plate with a turbulent boundary layer inlet profile. The working regime of the bleed system is, in this case, similar to a porous bleed installed upstream of a shock. Thus, the influence of the bleed parameters for supersonic conditions is investigated. The Mach number is fixed to a value of $M = 1.6$, which is also chosen for the later investigation with a shock-boundary layer interaction, where a shock-induced flow separation is investigated.

(a) Domain for the numerical investigation　　　**(b) Schematic of the hole pattern**
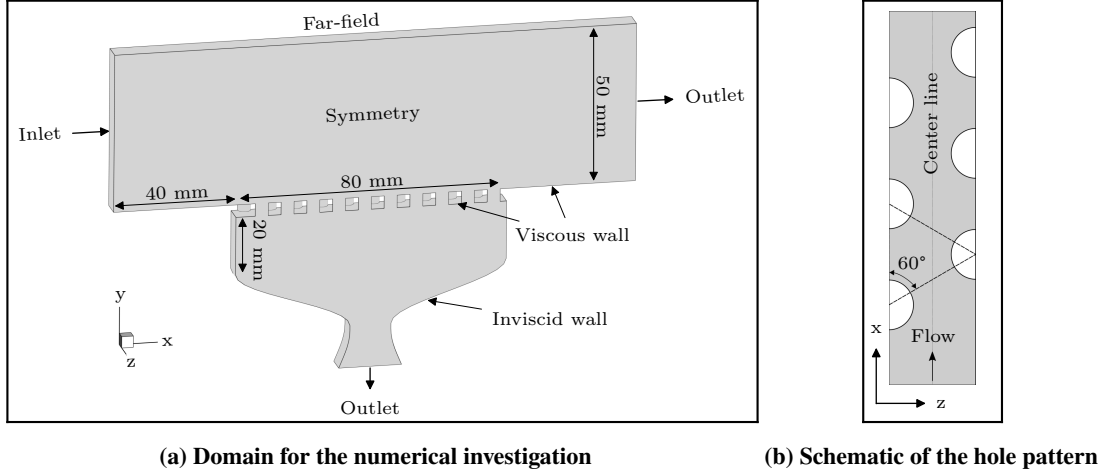
Fig. 2　Computational domain for the supersonic boundary layer bleeding

Fig. 2 illustrates the flow domain. The investigated bleed region starts with an offset of 40 mm from the inlet and has a length of 80 mm; its width depends on the bleed parameters and corresponds to the spanwise distance between two holes. The base area of the plenum is equal to the bleed region's area, and its depth is 20 mm. Below the plenum, a choked convergent-divergent nozzle is added to fix the plenum exit mass flow rate. The throat ratio

$$TR = \frac{A_{pl,ex}}{A_{bl}} = \frac{A_{pl,ex}}{\phi A_p} \tag{1}$$

is introduced to compare different bleed parameters for identical conditions. It is the ratio of the areas of the nozzle throat A_{throat} and the bleed region A_{bl}, which is, in turn, a function of the porosity level ϕ and the plate area A_p. Thus, the working regimes for all plates are assumed to be equal if the throat ratio remains constant.

The physical conditions are listed in Tab. 1, with the boundary layer quantities extracted directly upstream of the bleed region. All walls near the bleed holes and within the holes are handled as viscous/no-slip walls. Only the plenum sidewalls correspond to inviscid/slip walls since the influence on the mass flow rate is assumed to be negligible.

B. Porous bleed interacting with a strong shock

Again, the incoming Mach number is $M = 1.6$, and the bleed system is integrated into a flat plate. The physical properties are equal to the supersonic boundary layer bleeding (see Tab. 1). Here, the freestream flow is generated using a convergent-divergent nozzle. The nozzle shape is equal to that of the S8Ch wind tunnel at ONERA in Meudon for a later comparison of the numerical results with experiments. With the aim of investigating the interaction of the porous bleed with a strong shock, a shock generator is added to the domain. Here, the shock generator provokes an oblique shock which is non-regularly reflected at the wall, leading to a strong shock near the wall. Its presence allows us to investigate the bleed in supersonic and subsonic regimes.

The domain, including the shock generator, is schematically shown in Fig. 3. Here, the length of the bleed region is reduced to 40 mm to avoid any influence of the expansion fan while its width remains the same as in the first problem. The bleed region starts 40 mm downstream of the nozzle exit, where the leading edge of the shock generator is located. To obtain a shock system as drafted in Fig. 3, the shock generator's angle of attack is found to be $\alpha = 10°$. The shape of the shock generator is handled as a viscous wall.

3

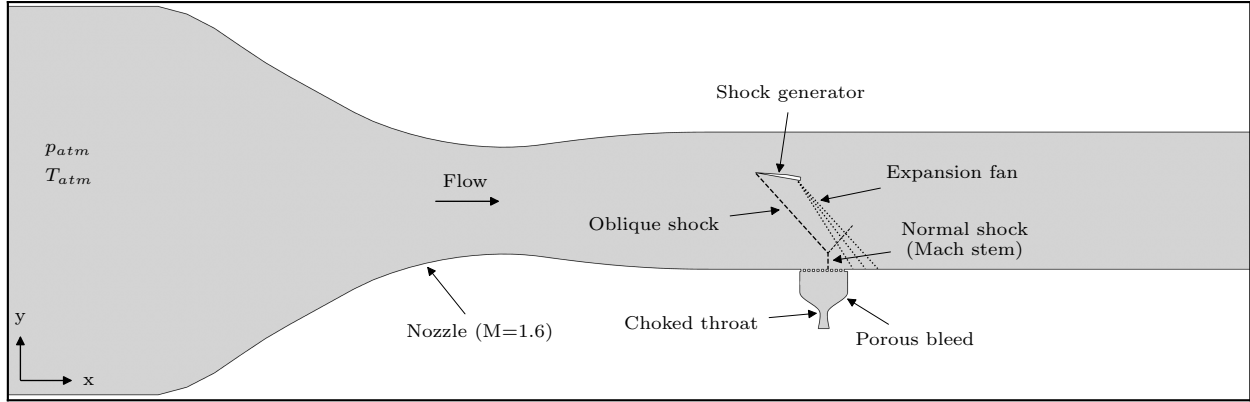**Fig. 3   Computational domain for the shock-boundary layer interaction**

IV. Numerical methodology

A. Geometry and mesh

The structured mesh is generated using the in-house pre-processing tool and mesh-generator **Cassiopee** [22]. A fully parameterized mesh allows the variation of the bleed parameters. Therefore, each hole is modeled out of five blocks using a butterfly mesh. The four other blocks are part of a C-grid, including the wall boundary layer on the plate and plenum sides (see Fig. 4). For an accurate resolution of the boundary layer, the minimum wall-normal cell size is $y^+ \approx 1$ (0.2×10^{-3} mm). Inside the holes, the wall is equally meshed. The cell-to-cell growth ratio is 1.1, which has been found to be the maximum value to accurately predict the local mass flow rate thanks to a preliminary mesh sensitivity study. The total number of cells is between 2.6 M and 20.6 M for the supersonic turbulent boundary layer bleeding and between 1.9 M and 11.6 M for the simulations with shock-boundary layer interaction.

B. Flow solver

The compressible Navier-Stokes equations are numerically solved using the ONERA-Airbus-Safran finite-volume solver **elsA** [23]. The Spalart-Allmaras turbulence model with quadratic constitutive relation [24] is applied. The second-order Roe upwind scheme utilizing the minmod limiter and the Harten entropic correction was used for the spatial derivative with a backward-Euler implicit local time-stepping scheme. A supersonic turbulent boundary layer profile is set as the inlet. The plenum exit area and the main outlet are supersonic outlets, while the far-field boundary condition is applied at the top of the domain. The domain is limited using a symmetry plane boundary condition on the
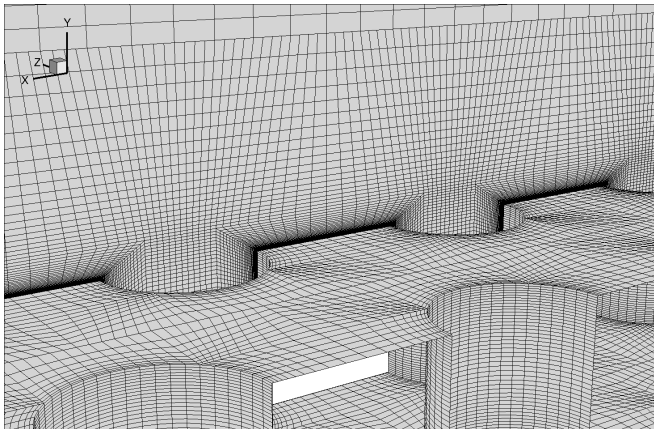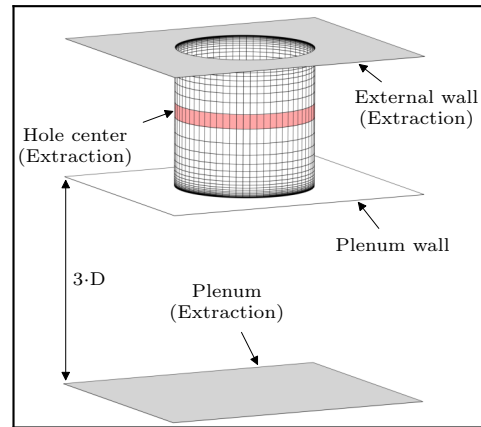

Fig. 4   View on mesh around the holes

Fig. 5   Positions for the local extractions

4

front and back.

C. Extraction and evaluation of the bleed mass flow rate

The mass removing efficiency by applying porous bleed systems is typically quantified by the surface sonic flow coefficient,

$$Q_{sonic,w} = \frac{\dot{m}_{bl}}{\dot{m}_{sonic,w}} \tag{2}$$

where the surface sonic mass flow rate $\dot{m}_{sonic,w}$ normalizes the (global) bleed mass flow rate $\dot{m}_{bl}$. The surface sonic mass flow rate can be computed using the static flow quantities at the wall as follows:

$$\dot{m}_{sonic,w} = p_w A_{bl} \left(\frac{\gamma}{RT_w}\right)^{1/2} \left(\frac{\gamma+1}{2}\right)^{-\frac{\gamma+1}{2(\gamma-1)}} \tag{3}$$

With the aim to analyze the local mass flow rate for each hole, the local extraction of the hole mass flow rate $\dot{m}_h$ and the local wall pressure is required. In the current study, the mass flow rate is extracted locally in each hole instead of using the bleed mass flow rate extracted at the plenum exit area. Therefore the flow momentum in the plate's normal direction is integrated

$$\dot{m}_h = \int \rho v dS \tag{4}$$

at half the thickness of the plate, which corresponds to the hole center, as illustrated in Fig. 5. The (global) bleed mass flow rate can then be easily computed by summing all hole mass flow rates:

$$\dot{m}_{bl} = \sum \dot{m}_h \tag{5}$$

Please note that Eq. 2 is adapted to local conditions by applying the hole mass flow rate.
The static wall pressure cannot be extracted at the hole position since its value is disturbed by the local velocity field around the holes. Therefore, a patch around the hole is defined with its size equivalent to the distance between the holes in the stream- and spanwise directions (see Fig. 5). On the patch, the average value of the static wall pressure is extracted. A similar method is applied to the static pressure in the plenum where the patch is equal in size but placed three hole diameters below the wall instead of using the wall pressure, which can be highly affected by the underexpanded jet at the hole exit. Higher patch distances lead to local information losses as the plenum pressure becomes more uniform with further distance from the holes. The plenum pressure is required to calculate the pressure ratio between the plenum and wall.

V. Supersonic turbulent boundary layer bleeding

CFD simulations have been performed for different hole diameters, porosity levels, and length-to-diameter ratios over a range of throat ratios to investigate the parameter influence on the mass flow rate and the supersonic turbulent boundary layer.
Fig. 6 presents the flow field inside the bleed holes, the cavity plenum, and externally of the bleed. The configuration has a hole diameter of $D = 2$ mm, a length-to-diameter ratio of $L/D = 1$, and a porosity level of $\phi = 22.67\%$. The flow field on the symmetry plane is shown in Fig. 6a. The gray patches show the out-of-plane holes located at another spanwise position. A strong impact of the bleed holes on the flow inside the boundary layer is apparent, where the mass removal induces expansion fans, which, in turn, cause a bending of the flow towards the wall. The holes capture the flow close to the wall, which is sucked into the cavity.
The zoom-in in Fig. 6a illustrates the typical flow structure in a supersonic (upstream) bleed. An expansion fan is provoked at the leading edge of the hole, which redirects the flow into the hole. Downstream, the flow is decelerated as the hole wall at the rear creates a back pressure, which results in the appearance of a shock. The so-called barrier shock penetrates, similar to the expansion fan, into the boundary layer. As a result, the flow inside the boundary layer passes several expansions and compression waves. Downstream of the shock, the flow is redirected towards the hole exit, and the low pressure inside the plenum causes an acceleration of the flow to supersonic conditions. Further downstream, an underexpanded jet emitting into the plenum is apparent. The mass flow rate passing the bleed hole is limited by the minimum size of the stream tube, the so-called vena contracta area. Its position is roughly at the imaginary intersection of the barrier shock with the (lower) outer streamline of the captured flow. Close to the front of the hole, flow separation
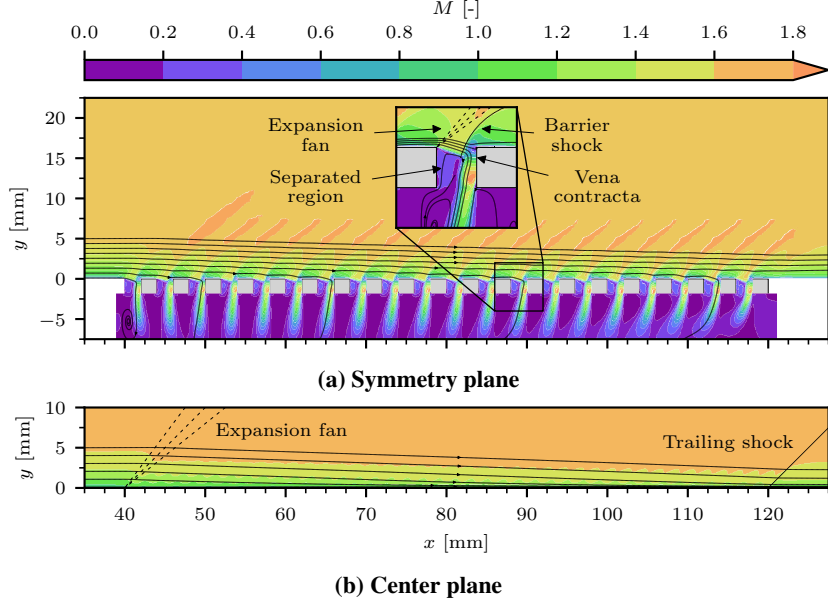
(a) Symmetry plane

(b) Center plane

Fig. 6 Mach number field for a supersonic turbulent boundary bleeding; gray patches illustrate the out-of-plane holes

is apparent, and flow enters the hole from the plenum side.

Fig. 6b shows the flow field on the center plane, located at another spanwise position between the two rows of holes (see Fig. 2b). The wall at this position is completely solid, which means that no holes are located on this plane. However, the effect of the expansion fans and barrier shocks provoked by the holes is evident. The first hole generates a particularly distinctive expansion fan which causes a strong flow deflection. Downstream, the out-of-plane effects of the holes are apparent. The flow passes several expansion and compression waves induced by the flow into the holes located out of the plane. Moreover, a trailing shock at the end of the plate is prominent, which is the barrier shock of the last hole, redirecting the flow into the wall-parallel direction. The slope of the streamlines clearly demonstrates the thinning of the boundary layer.

A. Hole diameter effects

First, the influence of the hole diameter is examined. Hereby, the porosity level is kept constant to $\phi = 22.67\,\%$ and the length-to-diameter ratio $L/D = 1$ for all diameters. The investigated hole diameters are in the range of $D = 0.25$ mm to 4.0 mm, which corresponds to ratios of diameter to boundary layer thickness of $D/\delta_{99} = 0.06$ to 0.90 and ratios of diameter to displacement thickness of $D/\delta_1 = 0.44$ to 7.02.

1. Near-field analysis for $TR = 0.7$

The flow fields inside the holes are shown in Fig. 7 for a throat ratio of $TR = 0.7$. From left to right, the hole diameter increases, and going from top to bottom corresponds to a shift in the streamwise direction. The different positions are illustrated in the schematic on the left. The first position corresponds to the first hole, the second position is slightly downstream, and the last position at almost two-thirds of the plate length. Both axes are normalized by the hole diameters to check if a self-similarity can be found.

The observation of the first row reveals significant differences in the flow field. The smaller the hole diameter, the lower the captured momentum is. The maximum mass flow rate passing the hole is fixed by the hole area, which is, in turn, a function of the hole diameter. Thus, small holes enable only the removal of flow in the near-wall region of the boundary layer where velocity and momentum are low. For the maximum diameter of $D = 4$ mm, the sonic line is relatively close to the wall, illustrating the high momentum. A strong expansion fan is observable, and the maximum Mach number inside the hole is higher than for smaller diameters.

The second row shows the holes at the position $x = 48$ mm. The flow fields are more similar in all cases, as seen
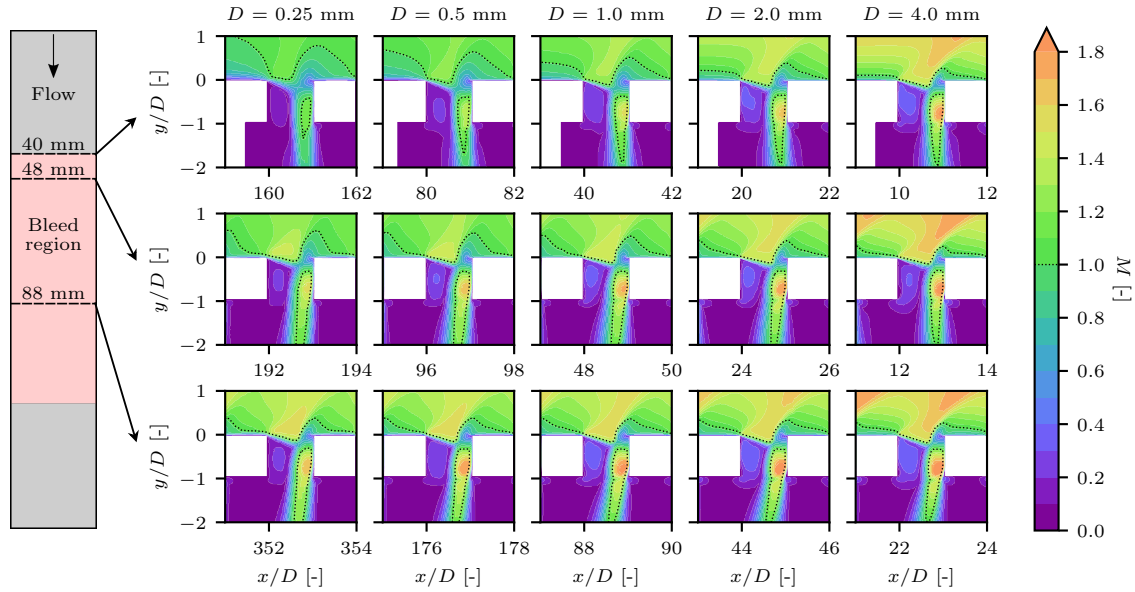
6

Fig. 7 Mach number contours of the flow in the bleed holes at $x = 40\,\text{mm}$, $48\,\text{mm}$ and $88\,\text{mm}$ (top to bottom)

by the position of the sonic line upstream of the hole. The main difference is the shock intensity since the upstream Mach number is again a function of the hole size. In the last row, the differences are even smaller, and the flow looks self-similar. The course of the sonic line looks equal, and only the external Mach number is higher for large diameters, which is a result of the larger field of view.

For a better comparison, the sonic lines are extracted and compared in Fig. 8a. This allows us to check the self-similarity
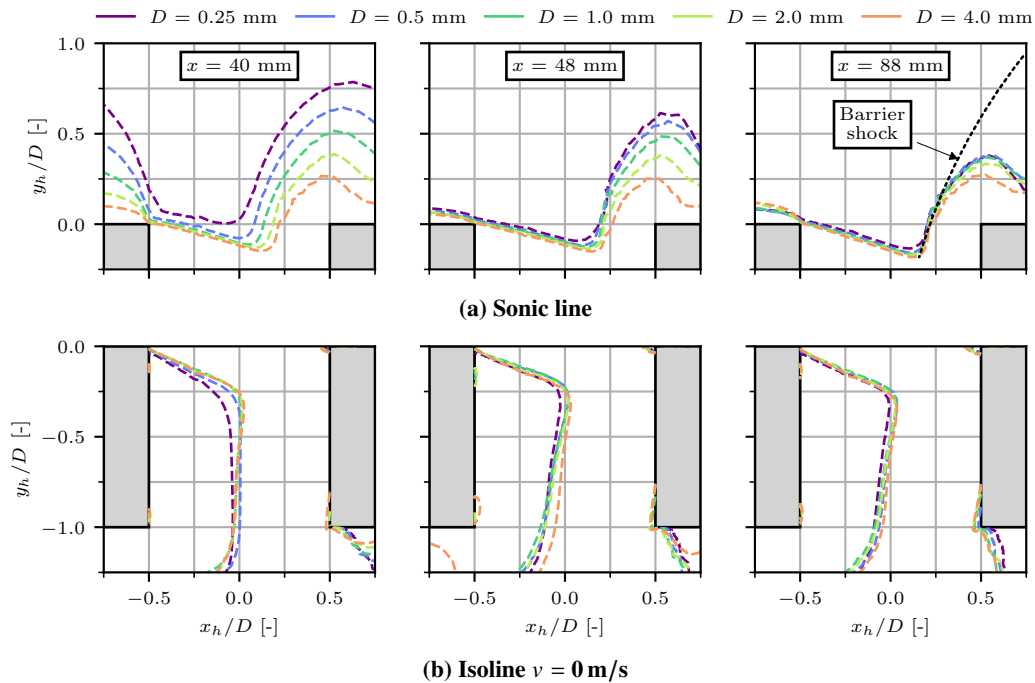

(a) Sonic line

(b) Isoline $v = 0\,\text{m/s}$

Fig. 8 Characteristic flow features of the flow in the bleed holes for different hole diameters at $x = 40\,\text{mm}$, $48\,\text{mm}$ and $88\,\text{mm}$ (left to right)

of the flow field for different hole diameters. Here again, significant differences are apparent for the first hole: The higher the hole diameter, the smaller the wall distance of the sonic line. Moreover, the barrier shock (see Fig. 1) is located closer to the trailing edge of larger holes, which is a consequence of the higher Mach number upstream of the shock, and thus, the higher pressure rise.

By going 8 mm downstream, a similarity of the incoming boundary layer can be observed. The incoming sonic lines lie almost on top of each other. The wall distance is only slightly higher for small diameters, resulting in a lower momentum of the captured flow. Thus, the barrier shock is still at another streamwise position. Besides, the boundary layer downstream of the hole becomes fuller since the sonic line moves closer to the wall than after the first hole. This effect is more pronounced for small hole diameters.

Remarkable is the trend of the sonic lines at $x = 88$ mm. The curves fit almost perfectly, and only for the highest hole diameter of $D = 4$ mm, a small deviation is apparent. Consequently, it can be concluded that the hole diameter strongly influences the thinning of the boundary layer. After a certain plate length, a similarity in the course of the sonic line is found in the normalized coordinate system, which means that the sonic lines are closer to the wall if the diameter of the hole is smaller. To the author's knowledge, no bleed model exists, which takes this effect into account even though it strongly affects the flow behavior in case of an adverse pressure gradient, e.g., induced by a shock.

In the second plot of Fig. 8, the isoline of zero transpiration velocity is extracted, allowing us to estimate the size of the separated region. Akatsuka et al. [4] assume a larger separated region if the ratio of D/δ increases as the momentum of the captured flow is higher. The observation of Fig. 8b partly confirms this assumption. A variation of the vena contracta area (see Fig. 1) in the first hole is apparent. The smaller the hole, the larger the vena contracta is. Thus, a higher mass flow rate is expected. However, by moving in the downstream direction, the isolines collapse. Only for the smallest diameter of $D = 0.25$ mm, the vena contracta area is still larger. As stated before, a stronger thinning of the boundary layer is achieved for small holes. Consequently, the ratio of D/δ decreases with the length of the plate. At a certain point, the momentum of the captured flow is almost similar, and hence, the vena contracta area becomes similar.
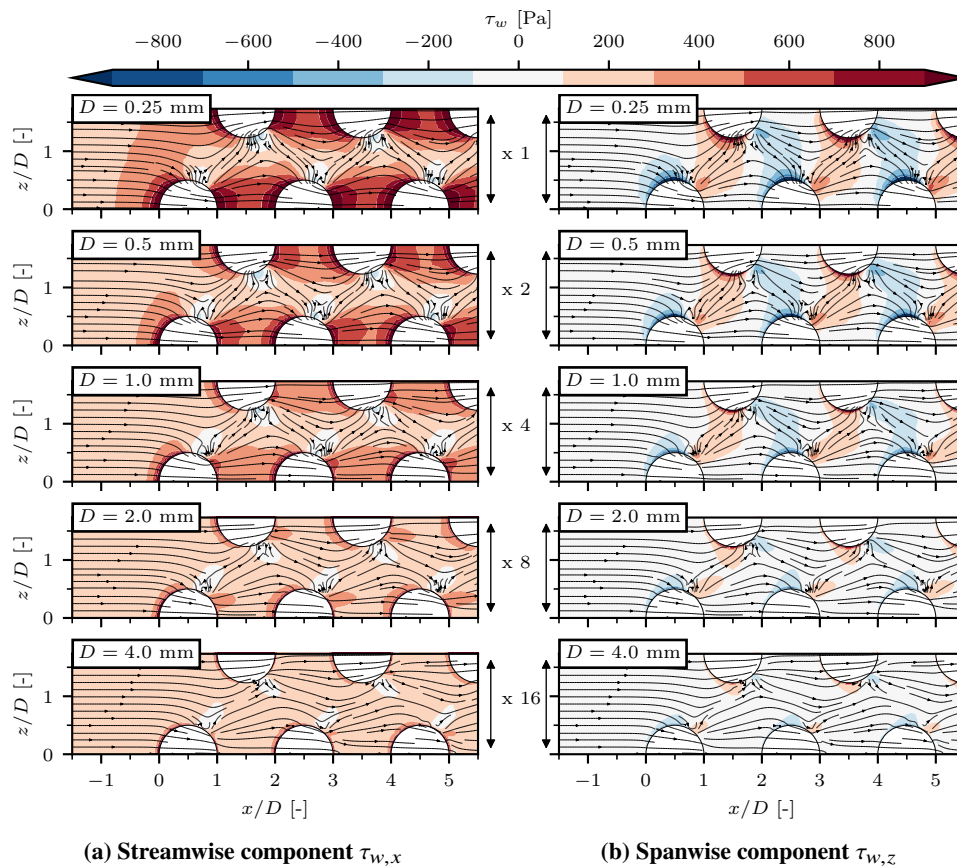

(a) **Streamwise component** $\tau_{w,x}$ (b) **Spanwise component** $\tau_{w,z}$

Fig. 9   **Wall shear stress at the beginning of the bleed region for different hole diameters**

Fig. 9 illustrates the wall shear stress in the streamwise (Fig. 9a) and spanwise directions (Fig. 9b) and the friction lines for varying hole diameters around the first five holes. From top to bottom, the hole diameter increases by a factor of two per plot. The coordinates are again normalized by the hole diameters to check similarities.

A view on Fig. 9a confirms the stronger thinning of the boundary layer for small diameters, with the wall shear stress between two succeeding holes being significantly higher. Strong variation of the wall shear stress is nevertheless observed in the holes' vicinity, with the shear stress being reduced by almost one order of magnitude on the centerline between two rows of holes.

Also, the shear stress in the spanwise direction (Fig. 9b) is larger for small diameters. It seems that small diameters provoke a more uniform suction in all directions. This can be seen by observing the friction lines, which are more curved for small diameters. While all friction lines are captured by the first two holes for small diameters, the incoming flow on the centerline is not captured by any hole for $D = 4\,\text{mm}$. Thus, the flow is assumed to be more homogeneous in the spanwise direction for small holes as the transversal removal of air is enhanced.

The displacement and momentum thickness, as well as the shape factor, are drawn in Fig. 10. The values are extracted on the centerline between the two rows of holes (see Fig. 2b). On the first view of the displacement thickness (Fig. 10a), the influence of the hole diameter is evident. As already stated before, the thinning of the boundary layer is stronger for smaller holes. The same effect appears in Fig. 10b, where the momentum thickness is shown. Besides, it can be observed that the flow on the center plane is more homogeneous for small diameters. For larger diameters ($D \geq 1\,\text{mm}$), oscillations in the curves are apparent, induced by the (out-of-plane) holes.

(a) Displacement thickness
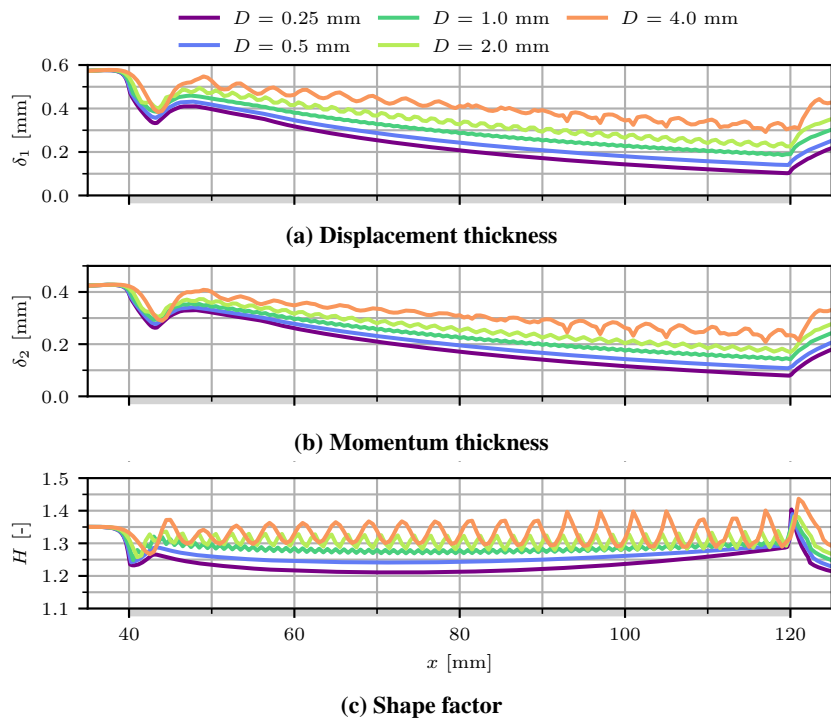
(b) Momentum thickness

(c) Shape factor

Fig. 10   Boundary layer characteristics for different hole diameters

Interestingly, the shape factor (Fig. 10c) is less affected by the hole diameter at the end of the bleed region, where its shape factor has an amount of $H \approx 1.3$ regardless of the hole diameter. Only at the beginning of the plate the shape factor tends to be smaller for small hole diameters. Moreover, out-of-plane effects are apparent for large holes, where the positions of the holes are locatable from the oscillations in the shape factor.

The external wall pressure is shown in Fig. 11 over the length of the porous plate. On the first grasp, a lower wall pressure is seen for small hole diameters. This effect is induced by the stronger thinning of the boundary layer. As a result, the expansion fan at the beginning of the plate is also stronger since the deflection angle must be higher. By going downstream, the pressure increases. As the thinning is not a linear trend but decreases with the position on the plate, as visible in Fig. 10, a continuous deflection is present, and thus, a continuous compression in the streamwise direction. At the beginning of the plate, a pressure drop is apparent from the first hole to the second, which is the consequence of
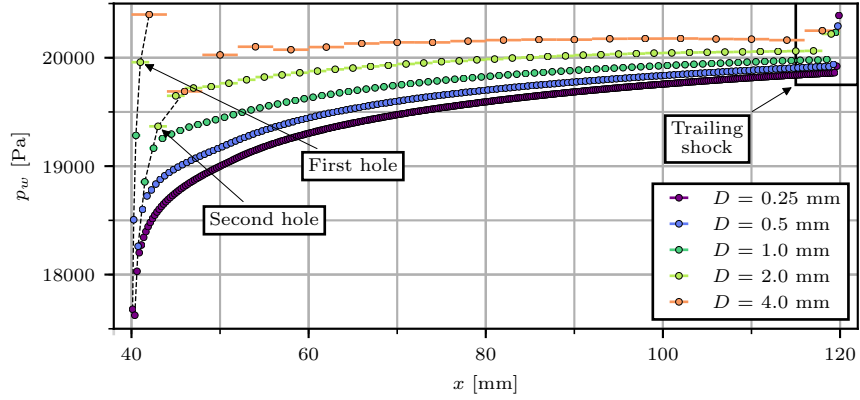
Fig. 11 External wall pressure over the bleed region for different hole diameters

the expansion fan located on the first hole. Since the wall pressure is extracted on a patch around the hole, the (larger) upstream pressure is also taken into account for the computation of the mean value.

A pressure rise can be found at the end of the plate (see the black frame on the right side of Fig. 11). This pressure rise is the consequence of the trailing shock on the end of the plate, where the flow is deflected into the wall-parallel direction. As the flow near the wall is subsonic, the pressure information can propagate upstream.

2. Analysis of the bleed efficiency

Fig. 12 shows the local surface sonic flow coefficient for different hole diameters as function of the pressure ratio of the bleed plenum and wall. One solid line represents here one simulation with one throat ratio. The right triangle (▶) illustrates the mass flow rate associated with the first hole, while the left triangle (◀) stands for the last hole and the circle (●) for the averaged value, i.e., the global plate working regime.
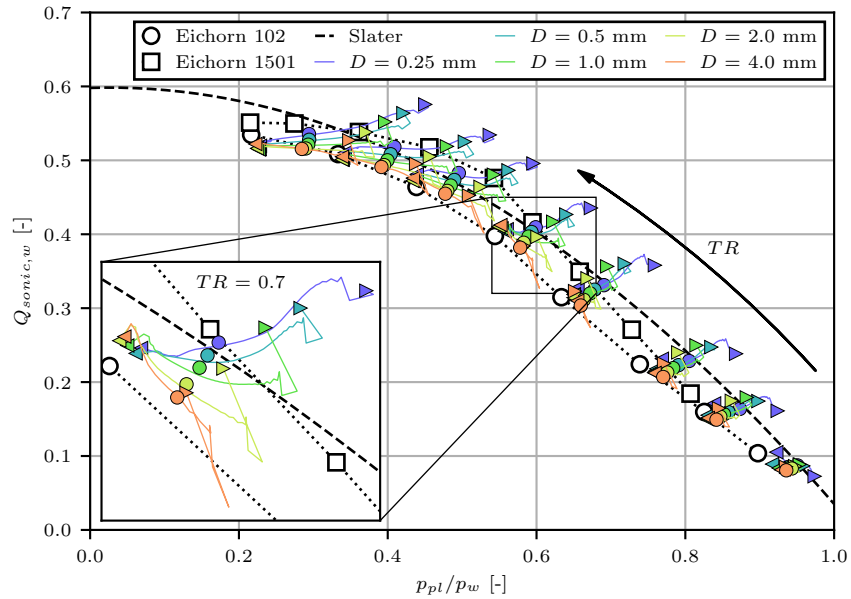

Fig. 12 Local surface sonic flow coefficients for various throat ratios

The general trend is similar for all hole diameters: The higher the throat ratio, the lower the pressure in the bleed plenum, and the higher the bleed mass flow rate. A second significant tendency in Fig. 12 is the drop of the pressure ratio with

10

the x-position on the plate. As stated before, the wall pressure increases with the length. Consequently, the pressure ratio p_{pl}/p_w decreases. The first hole is an exceptional case as the wall pressure is here higher because of the position of the expansion fan on the hole.

Also, the surface sonic flow coefficient varies with the position of the hole on the plate. The primary trend is the following: For small holes, the sonic flow coefficient decreases with the position on the plate as the vena contracta area gets smaller in size. For large holes, the sonic flow coefficient increases, which is probably a consequence of the smaller pressure ratio since the vena contracta area remains almost constant with the length. The effect of a varying sonic flow coefficient with the position is the strongest for medium throat ratios, where the transpiration flow is high, but the holes are unchoked, like the observed case with $TR = 0.7$ (see zoom in Fig. 12). For small throat ratios, where the pressure ratio is around $p_{pl}/p_w \approx 0.9$, the differences are less pronounced.

The convergence of the lines to the end of the plate confirms the similarity of the flow for all holes. Independently of the hole diameter, the last hole has a fixed sonic flow coefficient. Only for the smallest diameter of $D = 0.25$ mm, the flow coefficient is larger for high pressure ratios. On the contrary, the performance of the first hole depends on the hole diameter. As already stated, the vena contracta area differs for the diameters as D/δ_1 differs. As a result, small holes have a higher flow coefficient in the first hole. Moreover, in general, the first hole performs better in terms of efficiency as the inflow is undisturbed. In most cases, a drop in the efficiency is notable from the first to the second hole. This effect is more pronounced for large diameters and low pressure ratios, hence in cases where the first hole strongly influences the boundary layer.

The finding that the performance of the first hole strongly differs from the downstream lying holes is essential for the evaluation of former experimental studies. Bodner et al. [8], Davis et al. [9], Eichorn et al. [10] performed their experiments using a single hole only. Based on our results, the interaction of the holes needs to be considered as it affects the performance of the porous bleed.

The experimental data of two plates of the investigation of Eichorn et al. [10] is drawn. Plate 102 has a diameter of $D = 6.35$ mm and 1501 a diameter of $D = 0.794$ mm for an incoming boundary layer thickness of $\delta = 12.3$ mm and a displacement thickness of $\delta_1 = 2.41$ mm ($D/\delta_1 \approx 2.63$; 0.33) with a slightly higher Mach number of $M = 1.7$. The length-to-diameter ratios are $L/D = 1.125$ for plate 102, respectively $L/D = 2$ for plate 1501 and hence slightly higher than for the investigated plates. However, the experimental data shows the same trend of higher efficiency for
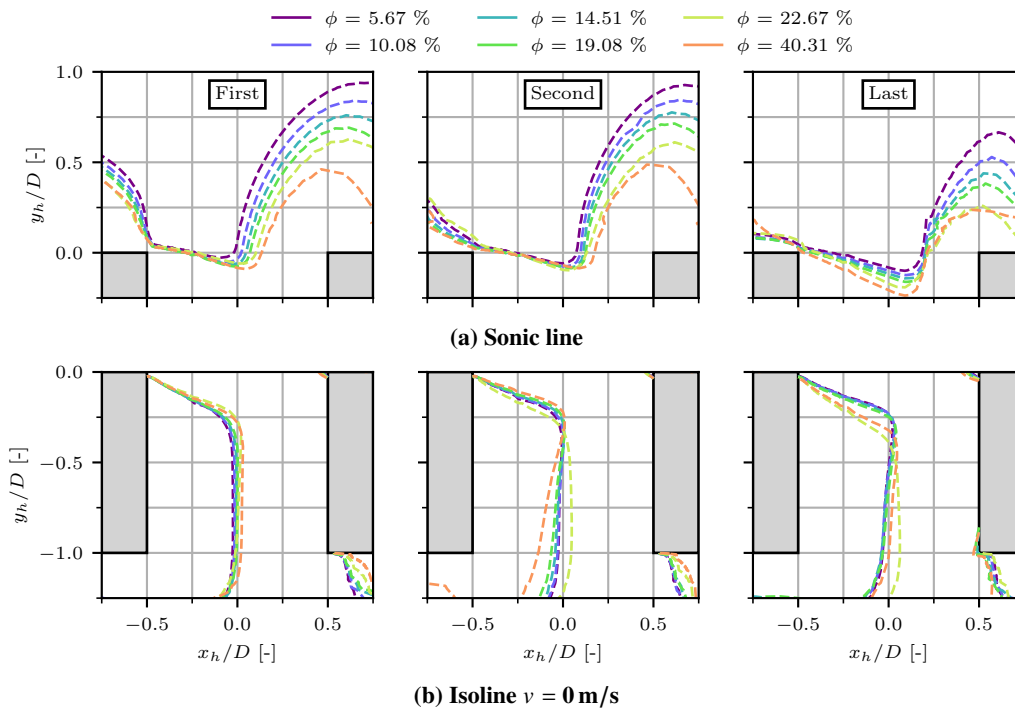

(a) Sonic line

(b) Isoline $v = 0$ m/s

Fig. 13 Characteristic flow features of the flow in the bleed holes for different porosity levels for first, second and last holes on the symmetry plane (left to right)

11

intermediate pressure ratios and low hole diameters.

The dashed black line shows the Slater's regression [14], which is not sensitive to the hole diameter. This regression is based on the experimental data of Willis et al. [2], acquired for a plate with a diameter of $D = 6.35\,\text{mm}$, a boundary layer thickness of $\delta = 21.0\,\text{mm}$, and a displacement thickness of $\delta_1 = 4.36\,\text{mm}$ ($D/\delta_1 \approx 1.46$) at $M = 1.58$. Both, the porosity level of $\phi = 19.1\,\%$, and the length-to-diameter ratio of $L/D = 1$ are similar. A closer look at the global plate performance ($\bullet$) reveals a good fit for the model with the smallest hole diameters, though the sonic flow coefficient is overestimated for large holes. Moreover, under choked conditions, the computed flow coefficient from the simulations is lower than the model's prediction.

B. Porosity level effects

The second investigated parameter is the porosity level ϕ. Again, the length-to-diameter ratio is fixed to $L/D = 1$; the hole diameter is chosen to be $D = 0.5\,\text{mm}$ to fulfill the typical ratio for air intake applications $D/\delta_1 \approx 1$ [20].

(a) Streamwise component $\tau_{w,x}$ (b) Spanwise component $\tau_{w,z}$
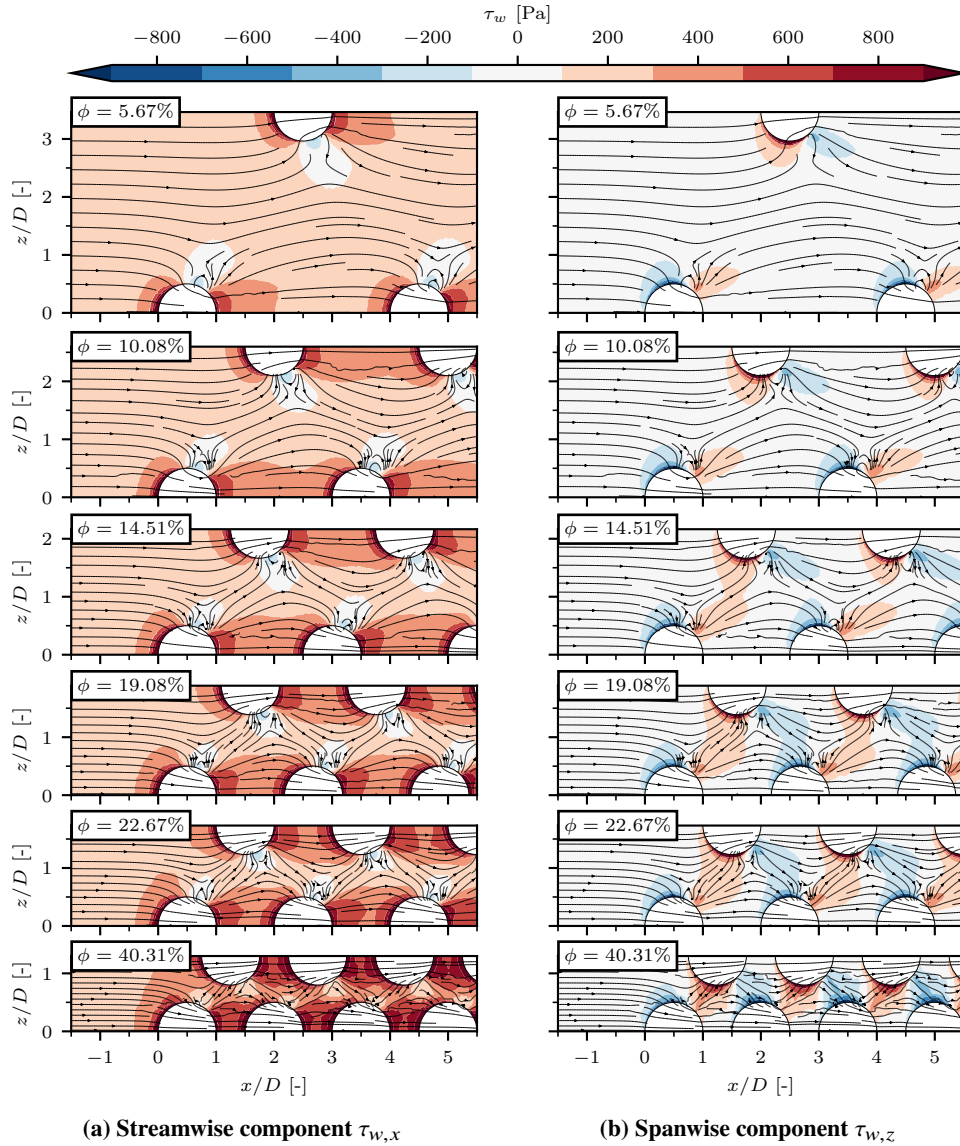
Fig. 14   Wall shear stress at the beginning of the bleed region for different porosity levels

1. Near-field analysis for $TR = 0.7$

Like in Sec. V.A, the sonic line, and the isoline $v = 0\,\text{m/s}$ are extracted and shown in Fig. 13 for a throat ratio of $TR = 0.7$. As the longitudinal hole positions are not equal for different porosity levels, the first, second, and last holes on the symmetry plane are presented here. Fig. 13a reveals large differences between the porosity levels. Already for the first hole, a significantly enhanced thinning of the boundary layer is found for the high porosity level because of the closer position of the sonic line to the wall. The barrier shock moves closer to the trailing edge for a higher porosity. Farther along the bleed, the position of the barrier shock converges for all cases. Nevertheless, some differences are still visible as the expansion fan is more pronounced for high porosity levels where the flow is strongly sucked into the hole. Fewer differences are seen in the size of the separated region in the holes (Fig. 13b). For high porosity levels, the vena contracta area is slightly smaller in the first holes. Towards the end of the plate, the size of the vena contracta area seems to be similar, but its position moves deeper into the holes. It seems that the pressure difference is larger for high porosity levels.

The wall shear stress at the beginning of the plate is presented in Fig. 14 for all investigated porosity levels. The streamwise component (Fig. 14a) reveals a strong effect of the porosity level: The higher the porosity level, the higher the wall shear stress. The explanation is the smaller distance between the holes, which effectively prevents the rethickening of the boundary layer. The effect is the strongest at the center between the two rows of holes where the wall is fully solid, regardless of the porosity level. For the lowest porosity level of $\phi = 5.67\,\%$, the wall shear stress at the centerline seems to remain constant.

Interestingly, the spanwise component (Fig. 14b) is less affected by the porosity level. Even for the highest and the lowest value, no increase, respectively decrease, is notable in the hole's vicinity. Also, the observation of the friction lines reveals only slight changes in the flow direction close to the wall. In contrast, the orientation of the friction lines rotates in the streamwise direction with further spanwise distance to the holes.

Fig. 15 illustrates the thinning of the boundary layer for the investigated porosity levels. The higher the porosity level, the stronger the thinning is. The different mass fluxes can explain this: If the porosity level is higher, the relative area of the holes is increased with respect to the porous plate area, and thus, more flow can be removed. Consequently, the thinning of the boundary layer, the expansion fan, and the compression caused by the deflection are stronger.
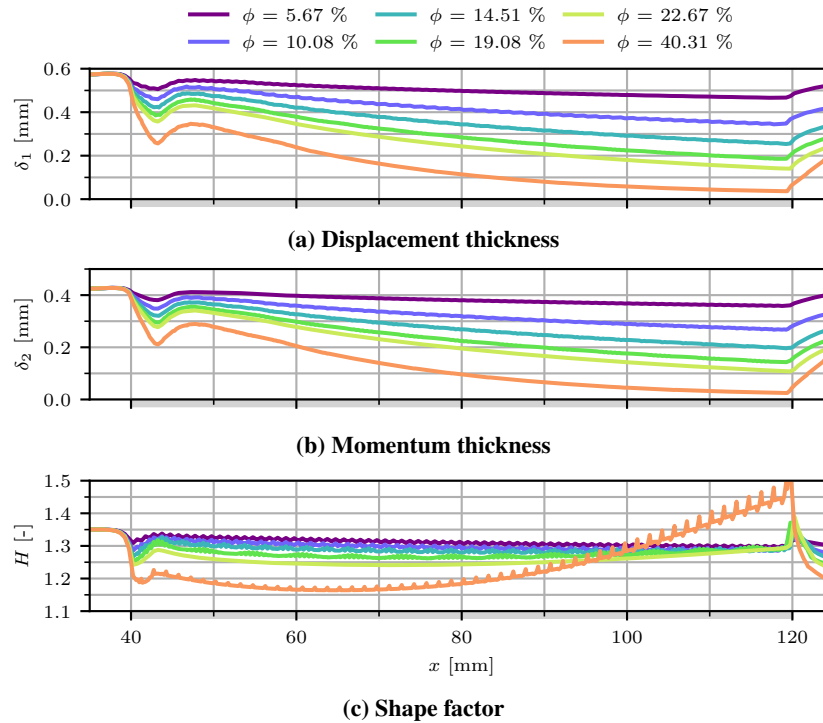

(a) Displacement thickness

(b) Momentum thickness

(c) Shape factor

Fig. 15   Boundary layer characteristics for different porosity levels

The porosity level significantly affects the shape factor, as shown in Fig. 15c. At the beginning of the plate, the boundary

layer profile is fuller for high porosity levels. As already stated, the distance between the holes is smaller. Hence, the effect of the holes on the centerline boundary layer is expected to be more remarkable. However, from a certain position, the shape factor increases. This position can be associated with some flattening of the displacement and momentum thickness curves, like if a limitation of the boundary layer thinning is achieved.

Fig. 16a compares the external static wall pressure for the different porosity levels. The higher the porosity level, the higher the boundary layer thinning is. Consequently, the expansion fan at the beginning of the plate is stronger, which results in a lower wall pressure. Downstream, the increase of the wall pressure is stronger for high porosity levels since the deflection is again larger.
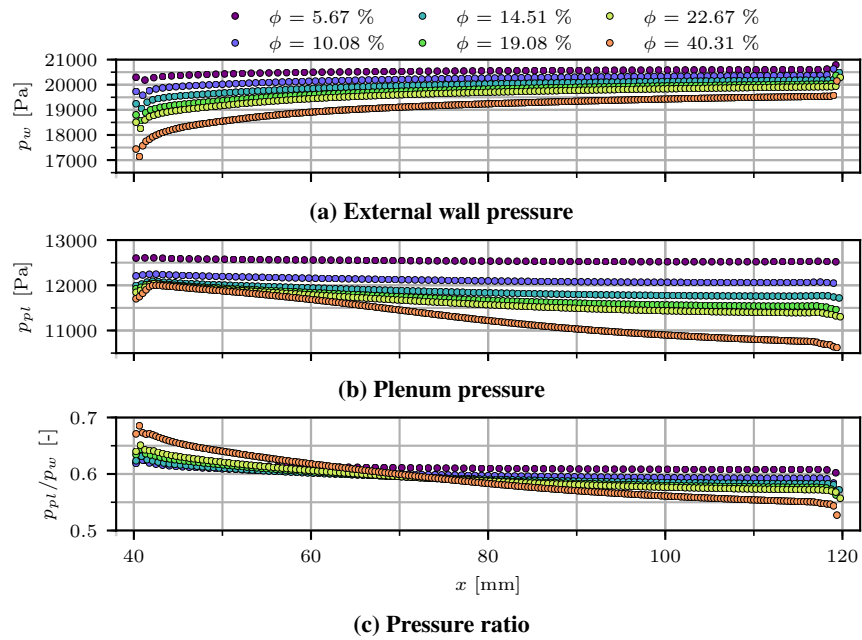

(a) External wall pressure

(b) Plenum pressure

(c) Pressure ratio

Fig. 16   Static pressure over the bleed region

Proportionally to the external wall pressure, the pressure inside the plenum changes (see Fig. 16b). The general trend is the opposite of the external wall pressure and decreases with the x-position. The pressure drop has a value of approximately half the pressure rise on the external side. The explanation for the pressure drop is that the total pressure decreases with the position on the plate because of the barrier shocks provoked by the holes. With the thinning of the boundary layer, the Mach number upstream of the barrier shock increases, which leads to higher total pressure losses inside the holes caused by the higher shock intensity. Consequently, the static pressure decreases as well. The higher the porosity, the higher the number of holes. Thus, the number of shocks and the shock intensity (stronger thinning) increase, which causes a higher plenum pressure drop.

The rise in the external wall pressure and the drop in the plenum pressure result in a change in the pressure ratio, as illustrated in Fig. 16c. The higher the porosity level, the higher the variation of the ratio with the position. However, the mean pressure ratio slightly decreases with the porosity level caused by the higher pressure losses as the number of holes and shocks increases.

2. Analysis of the bleed efficiency

The locally extracted surface sonic flow coefficient is compared to the model of Slater [14] in Fig. 17. The variation of the pressure ratio along the bleed is clearly shown. The higher the porosity level, the higher the horizontal distance between the first and last holes. Moreover, the effect is enhanced for large throat ratios where the drop in the total pressure along the x-position increases because of enhanced shock intensities with lower pressure ratios. A second trend is the decrease of the sonic flow coefficient with the position on the plate, which is caused by the growth of the separated region inside the hole as the momentum of the captured flow increases with the thinner boundary layer. Interestingly, the sonic flow coefficient slightly increases with the position on the high-porosity plates. It can be assumed that the
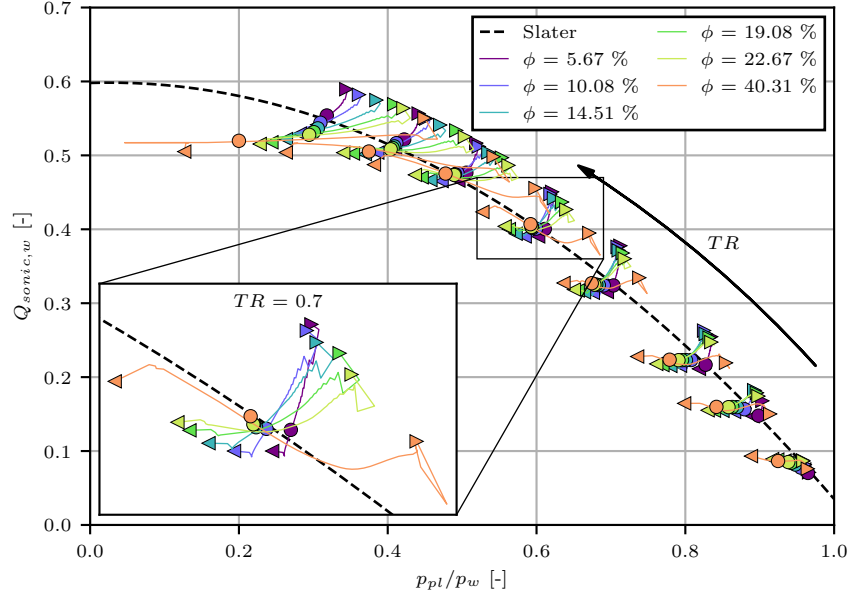
Fig. 17 Local surface sonic flow coefficients for various throat ratios

lower pressure ratio at the end of the plate leads to a slightly higher mass flow rate and hence to a slightly higher sonic flow coefficient.

Remarkably, all the points for the first holes seem to lie on one curve. This demonstrates that the first hole is mainly influenced by the diameter. In contrast to Fig. 12, the points for the last holes do not converge because the bleed mass flux, and hence the thinning of the boundary layer along the plate, are not similar.

Again, a good fit of the model of Slater [14] is observed for the global data and low porosity levels. With increasing porosity levels, deviations for low ($p_{pl}/p_w < 0.4$) and high ($p_{pl}/p_w > 0.7$) pressure ratios are apparent.

C. Length-to-diameter ratio effects

For the investigation of the length-to-diameter ratio, the porosity level is set to $\phi = 22.67\,\%$. The hole diameter is increased to $D = 1$ mm, aiming to reduce the computational costs. The length-to-diameter ratio L/D is varied in the range of 0.5 to 8.

1. Near-field analysis for $TR = 0.7$

Fig. 18 illustrates the influence of the length-to-diameter ratio on the static pressure for a throat ratio of $TR = 0.7$. On the first grasp, the low influence on the external wall pressure is evident (Fig. 18a). Note that the scale is the same as in Fig. 11. Thus, it can be concluded that the influence of the length-to-diameter ratio on the boundary layer is negligible. The same effect is found but not shown by analyzing the displacement and momentum thickness.

A different picture is found in Fig. 18b, where the static plenum pressure is illustrated. For high length-to-diameter ratios ($L/D \geq 4$), the plenum pressure is almost constant. For $L/D = 2$, the plenum pressure shows the same trend but lies at a lower level, and for smaller ratios, a pressure drop similar to Fig. 16b is observed. Since the length-to-diameter ratio is set to $L/D = 1$ for investigating the porosity level (see Sec. V.B), both effects are probably combined.

2. Analysis of the bleed efficiency

Fig. 19 shows the trend of the sonic flow coefficients with the pressure ratio. In addition to the model of Slater [14], the model of Harloff and Smith [20] is drawn as it considers the length-to-diameter ratio in the computation of the bleed mass flow rate. It is clearly seen that the latter model overestimates the sonic flow coefficient, especially for high throat ratios. However, it fits well with the results of the simulations with higher length-to-diameter ratios for low throat ratios. The drop of the plenum pressure for small ratios is significant as the pressure ratio strongly varies from the beginning to
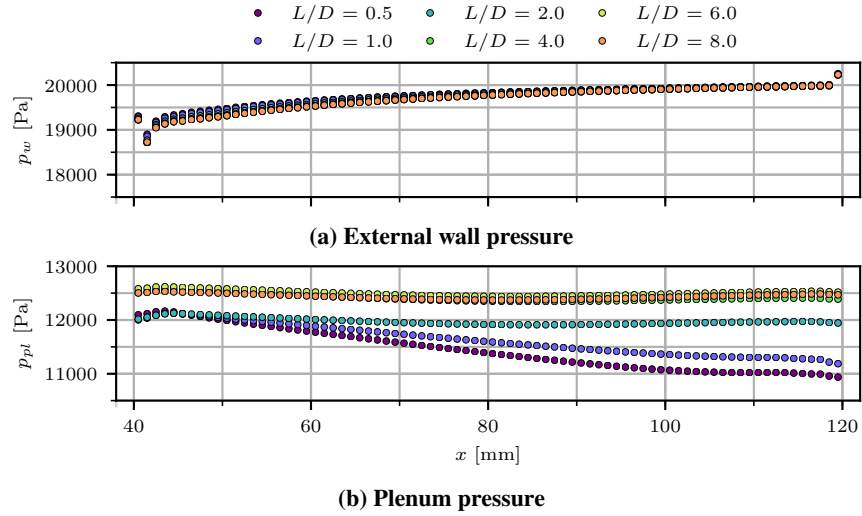
15

(a) External wall pressure

(b) Plenum pressure

Fig. 18 Static pressure over the bleed region for different length-to-diameter ratios

the end of the plate. Moreover, a degradation of the flow coefficient can be seen. For high pressure ratios $p_{pl}/p_w > 0.6$, the highest sonic flow coefficients are found for $L/D \geq 4$. Interestingly, also the pressure ratio is higher. Thus, it can be concluded that high ratios are more efficient. For smaller pressure ratios, high length-to-diameter ratios seem to be less efficient. Here, the sonic flow coefficient is smaller. For choked holes (high TR), an $L/D = 1$ is optimum.

Our findings do not support the assumption of Harloff and Smith [20] that an $L/D > 3$ leads to a degradation of the sonic flow coefficient. In contrast, higher length-to-diameter ratios seem to improve the performance of the porous bleed for unchoked conditions.

The sizes of the separated regions inside the holes are compared in Fig. 20 for the throat ratios $TR = 0.7$ (Fig. 20a) and $TR = 1.8$ (Fig. 20b) at different positions on the plate. The contour colors correspond with the lines and show the extension of the respective hole.

For unchoked conditions (Fig. 20a), a smaller vena contracta area for $L/D = 0.5$ is found independently of the position
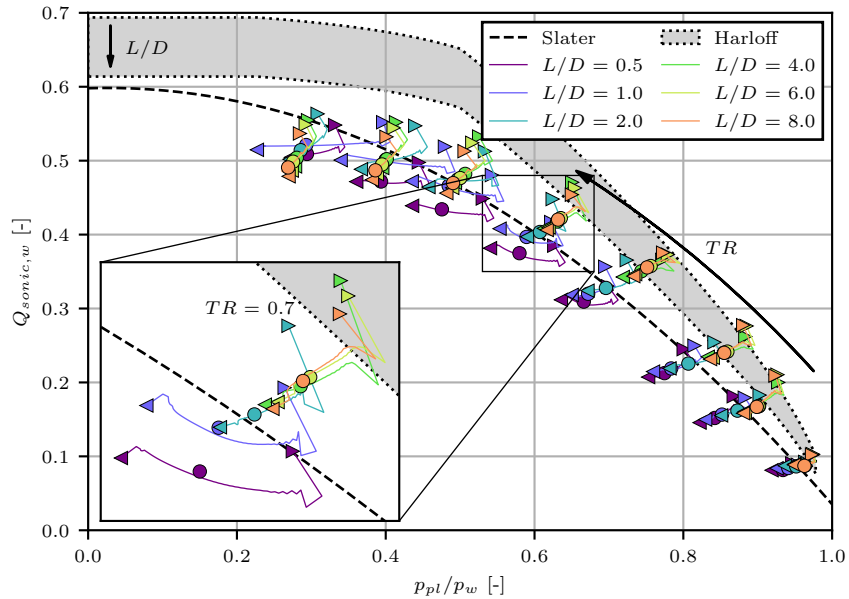

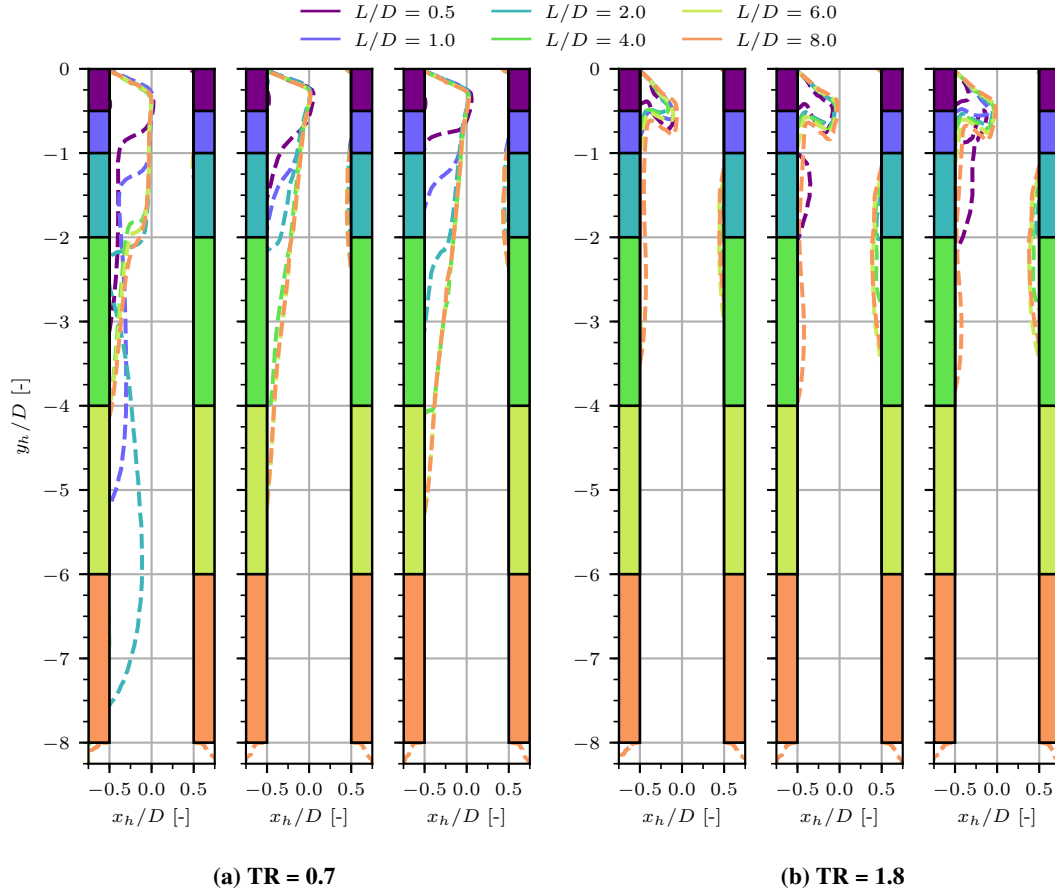**Fig. 19 Local surface sonic flow coefficients for various length-to-diameter ratios**

16

Fig. 20 **Size of separated region in the holes for different length-to-diameter ratios at** $x = 40\,\text{mm}$, $48\,\text{mm}$ **and** $88\,\text{mm}$ **(left to right)**

on the plate. The vena contracta area does not change significantly for larger ratios. However, with long holes, the jet inside the holes widens. For the first hole, the jet seems to be fully attached after approximately four hole diameters. Further downstream, this distance increases to slightly more than five diameters. In combination with Fig. 6, Fig. 18, and 19, it can be concluded that a fully attached flow at the hole exit leads to fewer pressure losses inside the cavity, as no flow enters the hole from the plenum side and a higher sonic flow coefficient. Moreover, an oversizing of the hole in the length has a lower impact than an undersized hole. Consequently, the pressure losses are more pronounced than the friction losses inside the hole.

Different behavior is found for a throat ratio of $TR = 1.8$ (Fig. 20b). Reducing the plenum pressure leads to an earlier flow reattachment inside the hole. Consequently, shorter holes are preferable as the friction losses are more pronounced, as shown in Fig. 19, where the pressure ratio is smaller. Moreover, the size of the vena contracta area seems to be smaller for larger length-to-diameter ratios, which explains the lower sonic flow coefficient.

VI. Shock-boundary layer interaction control

Like in Sec. V, CFD simulations have been performed for different hole diameters, porosity levels, and length-to-diameter ratios over a range of throat ratios. Here, the effect of the parameters on the control of the shock-boundary layer interaction is investigated.

The flow field is presented in Fig. 21 for a bleed configuration with a hole diameter of $D = 2\,\text{mm}$, a length-to-diameter ratio of $L/D = 1$, and a porosity level of $\phi = 22.67\,\%$. Fig. 21a shows the flow on the symmetry plane. A slight thinning of the supersonic boundary layer can be seen by following the streamlines upstream of the shock. After passing the shock, the streamlines are bent towards the wall, which indicates a high mass removal downstream of the shock where
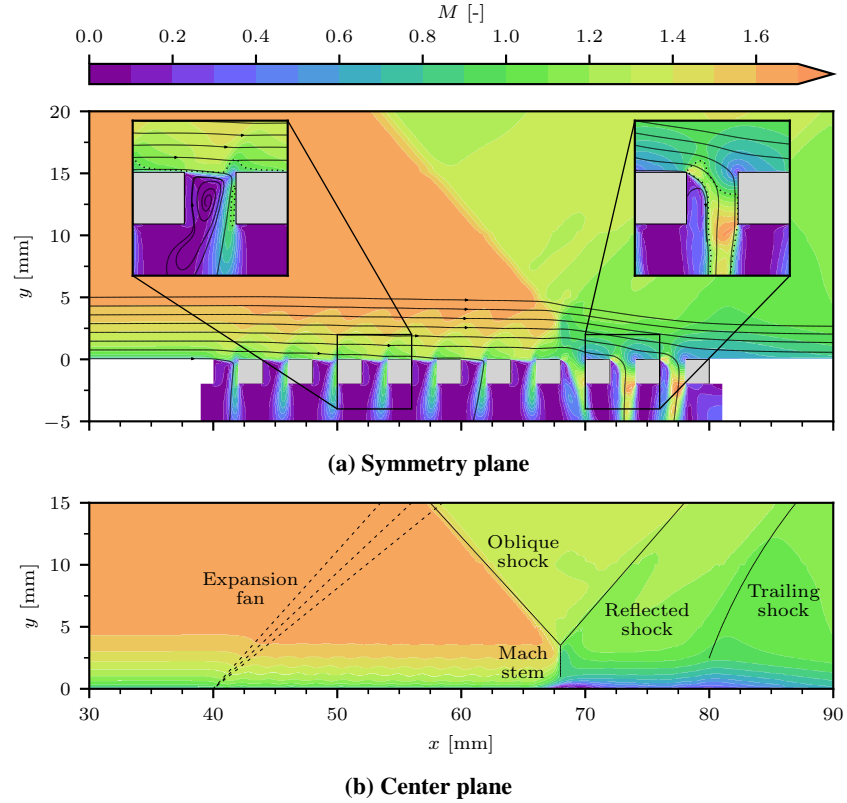
17

(a) Symmetry plane

(b) Center plane

Fig. 21   Mach number field for a shock-boundary layer interaction control; gray patches illustrate the out-of-plane holes

the flow is subsonic. No shock-induced flow separation is notable as the low-momentum flow is sucked into the plenum. The zoom on the left-hand side shows the flow field inside a bleed hole upstream of the shock where the external flow is supersonic. The suction rate in this region is relatively low, the holes are unchoked, and the flow inside the hole becomes only in a small area supersonic, as illustrated by the sonic line (dotted). Moreover, a sizeable separated region is observed.

A completely different flow field is apparent on the zoom on the right, presenting the flow inside the hole in the subsonic region downstream of the shock. Here, the external flow is subsonic. Thus, no barrier shock is evident, and the expansion fan is limited to a small area close to the leading edge, where the flow is accelerated to supersonic conditions again. It can be assumed that this effect is limited to a specific range of external Mach numbers. Below a certain limit, the external flow will be too low to accelerate to supersonic conditions around the leading edge. Consequently, no expansion fan will be present. The flow inside the hole is choked, as visualized by the sonic line. The separated region inside the holes in the subsonic region is significantly lower. Its size is strongly affected by the external Mach number and can be assumed to decrease for lower Mach numbers. Moreover, the streamlines directed towards the plate indicate a substantial thinning of the boundary layer.

The flow on the center plane is detailed in Fig. 6b, where the pattern of the shock reflection, as well as the expansion fan and the trailing shock induced by the porous bleed, are illustrated. In the supersonic region upstream of the shock, small out-of-plane effects caused by the hole located outside the plane are evident in the form of irregularities in the Mach number inside the boundary layer. Downstream of the shock, where the external flow is subsonic, no out-of-plane effects are apparent. Close to the shock, the Mach number in the vicinity of the wall is low, which indicates the presence of a small local flow separation.

A. Hole diameter effects

1. Near-field analysis for $TR = 0.7$

Fig. 22 shows the curves of the external wall pressure (Fig. 22a) and the surface sonic flow coefficient (Fig. 22b) over the bleed region. The shock position is located between $x = 65$ mm and $x = 70$ mm, as seen by the pressure rise in Fig. 22a. Upstream of the shock, the same behavior as shown in Sec. V.A is observed: The larger the hole, the higher the wall pressure. Moreover, the shock is more smeared for larger hole diameters. Hence, better control is achieved for small holes. Downstream of the shock, the differences are smaller. Only at the end of the plate, a larger pressure rise for tiny holes is found, leading to the assumption of a stronger trailing shock as the pressure information can spread upstream inside the boundary layer.
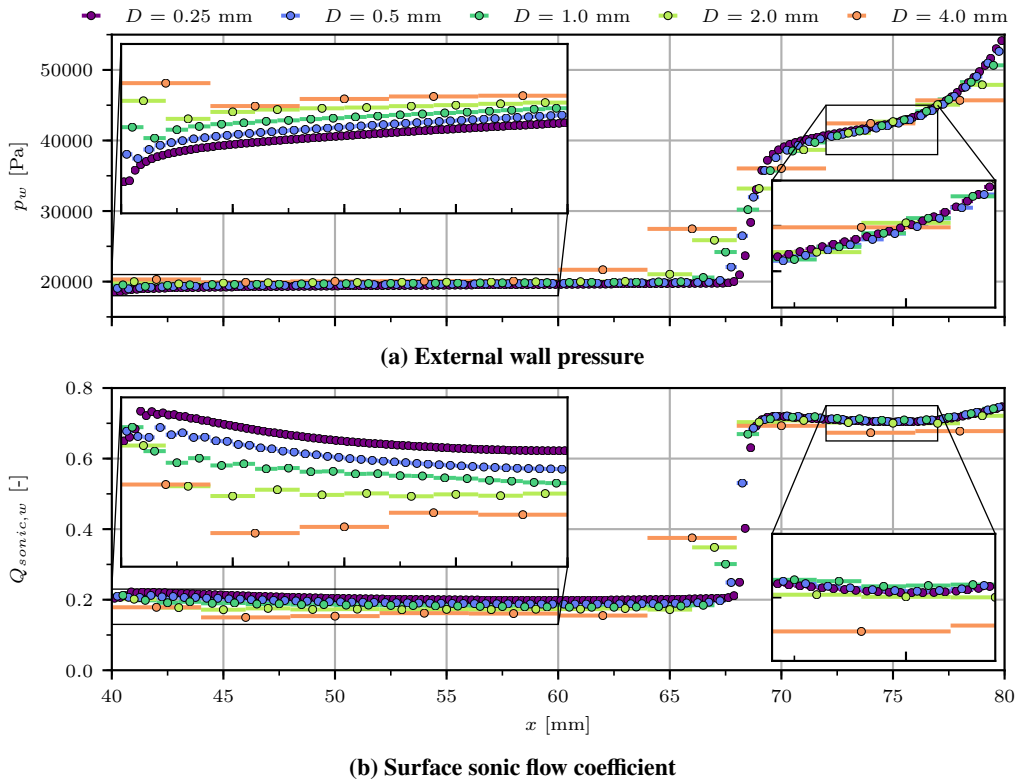

(a) **External wall pressure**

(b) **Surface sonic flow coefficient**

Fig. 22   Comparison of the flow quantities for different hole diameters in the shock-boundary layer interaction control

The surface sonic flow coefficient (Fig. 22b) behaves similarly to the wall pressure. Upstream of the shock, the flow coefficient is the highest for the smallest holes, and with further distance from the beginning of the plate, the lines merge, as seen in Sec. V.A. Passing the shock foot, the sonic flow coefficient sharply increases as the pressure difference from the external wall to the plenum increases. Downstream of the shock, a lower efficiency is found for the largest diameter of $D = 4$ mm. The differences between the other hole diameters are small.

The flow fields for the different hole diameters are shown in Fig. 23. On the left, the contours are extracted on the symmetry plane so that the flow inside the holes is visible. The flow on the center plane between the two rows is shown on the right side. From top to bottom, the hole diameter is increased. The gray patches illustrate the position of the second row of bleed holes.

A view of Fig. 23a reveals significant differences between the flow field. For the smallest diameter $D = 0.25$ mm, the flow field upstream of the shock is very homogeneous. There is no apparent penetration of the barrier shocks in the boundary layer. The shock is located at $x = 68.5$ mm (dotted vertical lines), and no lambda foot is found. This is a consequence of the strong thinning of the upstream boundary layer. Thus, the interaction of the shock with the boundary layer is effectively mitigated with no flow separation visible. Downstream of the shock, a strong transpiration flow is evident with the high-velocity jets in the plenum. As a result, no flow separation is apparent. At the end of the plate, the
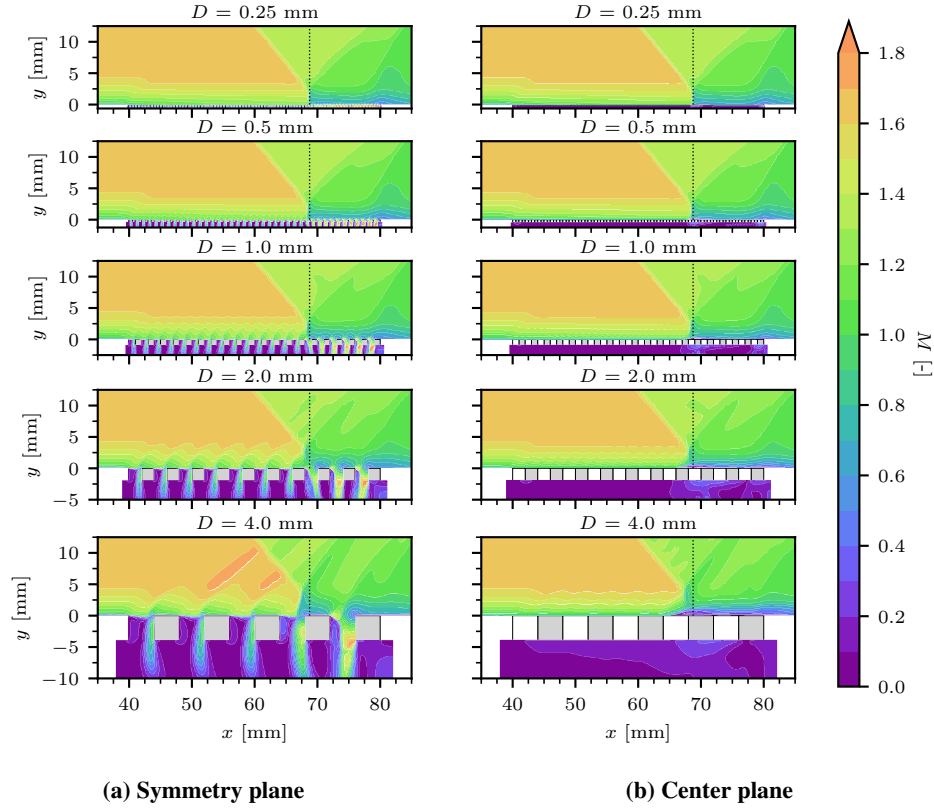
Fig. 23 **Mach number contours for different hole diameters; gray patches illustrate the second row hole positions**

trailing shock, which leads to a weak thickening of the boundary layer, is visible.

With larger hole diameters, a slight upstream displacement of the shock foot is apparent. Moreover, for hole diameters $D \geq 1.0$ mm, the flow field is less homogeneous, and a penetration of the barrier shocks through the boundary layer can be found. This also affects the shape of the shock wave, which is stronger bent in the vicinity of the holes. For the largest diameter of $D = 4$ mm, a strong interaction of the holes with the boundary layer can be observed. Every hole creates an expansion fan and a barrier shock that penetrate the boundary layer and the incoming oblique shock wave. The shock wave is curved, and the shock foot is approximately 3 mm further upstream than for the smallest holes. Also, downstream of the shock, differences can be noted: The boundary layer is thicker, and the trailing shock is less prominent. These findings indicate a lower bleed efficiency.

In Fig. 23b, the effect of the hole diameter is more significant. For small hole diameters $D \leq 1$ mm, the flow field looks identical to the left-hand side. This means that the flow field is very homogeneous in the spanwise direction. For larger holes $D \geq 2$ mm, the impact of the barrier shock and the expansion waves is evident. Moreover, the Mach number in the vicinity of the wall below the shock foot is very low. Here, a lambda shock foot is observable, which indicates the presence of local flow separation.

A more detailed overview of the control of the shock-induced flow separation is shown in Fig. 24, which displays the wall shear stress below the shock foot. Again, the streamwise (Fig. 24a) and spanwise (Fig. 24b) components are presented as well as the friction lines. The coordinates are not scaled to image the size of the separated region.

Fig. 24a gives an idea of the size of the separated region. For the largest holes of $D = 4$ mm, a separation line between the rows of holes at $x = 64$ mm is apparent. Downstream, negative values of wall shear stress are observed, which means that the flow streams in the upstream direction. Downstream of the holes, the flow is fully attached as we have a strong removal of low momentum through the holes. The size of the area with negative shear stress is roughly the streamwise distance between two holes (two diameters for this porosity level) times the spanwise distance between the hole edges of the rows. In other words, the adverse pressure gradient has the strongest impact on the area without holes, where the flow can not stream into the cavity to avoid undergoing the pressure rise.
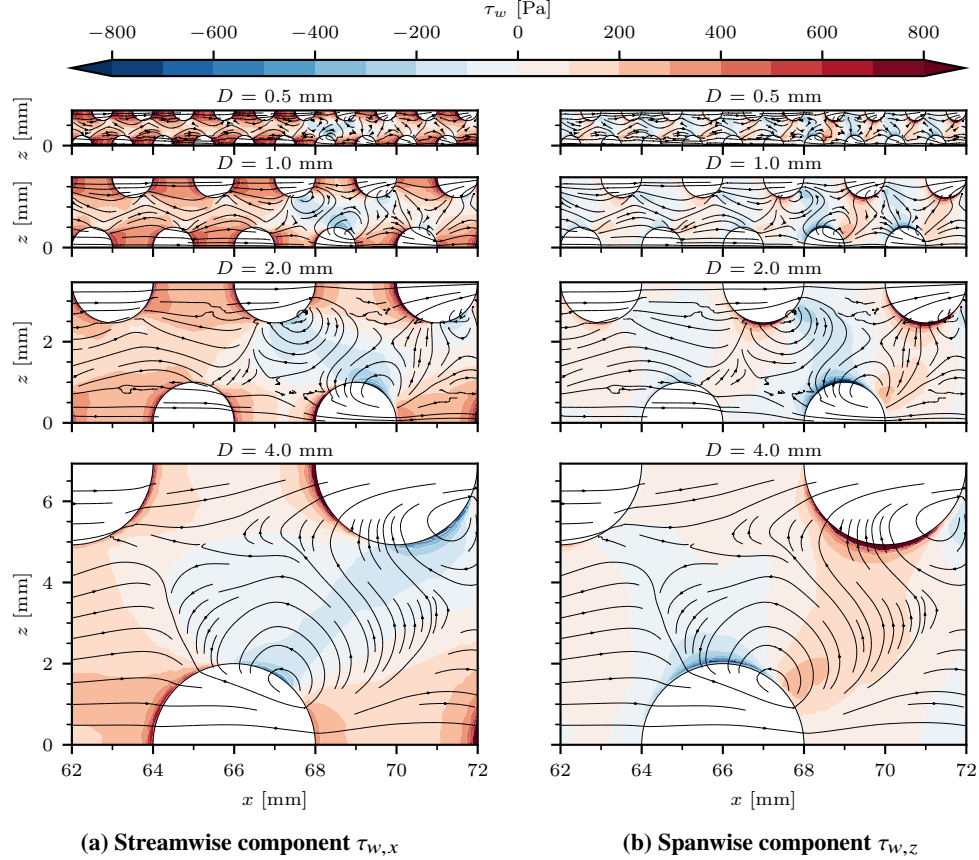
20

(a) Streamwise component $\tau_{w,x}$ **(b) Spanwise component** $\tau_{w,z}$

Fig. 24   Wall shear stress below the shock foot for different hole diameters

The same image is found for holes of $D = 2$ mm. The region of negative stresses has approximately the same extension in terms of diameters. However, the absolute size of the region is smaller as the diameter is only half the one of the previously regarded case. Moreover, the separation line moves downstream to $x = 66$ mm, which shows a better control of the shock-boundary layer interaction.

With decreasing hole diameters, the same effects are apparent. The separation line moves further downstream, and the streamwise extension of the region with negative shear stresses is still two to three hole diameters. Hence, the reattachment line is located further upstream. However, a clear determination of the reattachment is challenging. The high bleed mass flow rates combined with streamwise flow velocities can also lead to negative shear stresses slightly downstream of the holes.

Fig. 24b shows another effect occurring with a decrease in the streamwise flow velocity. Downstream of the separation line, the spanwise component of the shear stress increases. For conditions without external flow, the suction of the holes in combination with entrainment effects would lead to a uniform suction from all directions. All friction lines would stream into the holes where a sink could be found. The higher the flow velocity, the higher the part of captured air from upstream. As a result, the spanwise component decreases, as already shown in Fig. 9. Here, the normal shock decelerates the mean flow. Consequently, the spanwise component must increase. This effect weakens by moving downstream as a thinning of the boundary layer occurs, and the streamwise flow velocity increases again.

2. Analysis of the bleed efficiency

The surface sonic flow coefficient as a function of the pressure ratio is visualized in Fig. 25. Additionally, the bleed models of Slater [14] and Grzelak et al. [21] are shown. The latter is based on a numerical database of single-hole simulations without external flow and contains different parameter influences such as the length-to-diameter ratio and the porosity level. However, it must be noted that the calibrated range for the porosity level is from 4 % to 10 % and hence lower than the used porosity level in this investigation. Moreover, the minimal length-to-diameter ratio is $L/D = 1.5$.
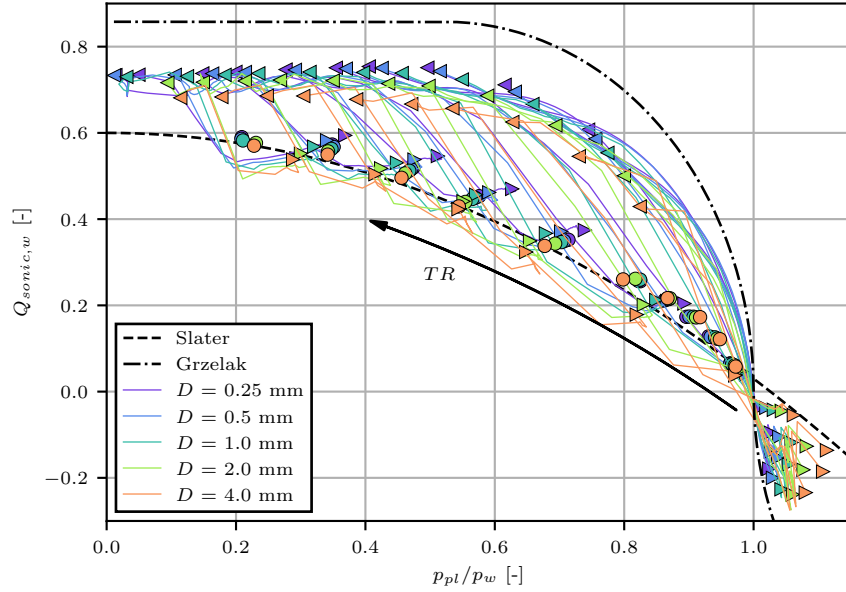
Fig. 25 **Variation of the surface sonic flow coefficient for different hole diameters for the shock-boundary layer interaction**

In comparison to the previous curves for the sonic flow coefficient, the trend for the shock-boundary layer interaction is more challenging to grasp on one view since an extensive range of working regimes is covered by one throat ratio. For low throat ratios, the plenum pressure can exceed the external wall pressure upstream of the shock. Thus, the air is not removed but added to the boundary layer (blowing). Thus, no thinning but a thicking of the boundary layer takes place. Downstream of the shock, the pressure ratio is higher regardless of the throat ratio. Thus, the sonic flow coefficient sharply increases. Since the flow momentum in the vicinity of the wall is low, the size of the separated region decreases, resulting in a larger vena contracta area and hence a higher flow coefficient than for the supersonic bleeding. On this plot, a diameter dependence on the flow coefficient is apparent. The higher the hole diameter, the lower the sonic flow coefficient is. However, the trend of the last holes is similar to the regression of Grzelak et al. [21] but lower as the external flow velocity is not zero ($M \approx 0.7$). Moreover, the choking of the holes below the critical pressure ratio of $p_{pl}/p_w = 0.528$ is evident. For lower ratios, the flow coefficient exhibits a plateau.

Interestingly, by observing the mean plate values, large holes are found to be slightly more efficient for low throat ratios. The sonic flow coefficient is equal for all cases, but the pressure ratio is higher. The reason seems to be the low blowing efficiency for large holes. For high throat ratios, small holes are preferable, as expected.

B. Porosity level effects

The influence of the porosity level on the shock-boundary layer interaction is shown in Fig. 26. Again, the sonic flow coefficients and the models of Slater [14] and Grzelak et al. [21] are illustrated. Generally, it must be noted that comparing different porosity levels is challenging as the global bleed mass flux strongly differs. The higher the bleed mass flux, the better the control of the shock-boundary layer interaction because of the higher momentum close to the wall. Fig. 26 still allows the comparison of the efficiency of different porosity levels.

For low throat ratios, blowing takes place upstream of the shock for all porosity levels with higher intensity for low-porosity plates. The reason is the weaker control of the shock. As a result, the location of the shock foot moves upstream, and the plenum pressure and the mass flow rate increase.

Downstream of the shock, the differences between the different porosity levels are minor. All points of the last holes show a similar trend. For unchoked conditions, high porosity levels seem to be slightly more efficient, whereas the contrary is the case for choked holes. Also, the findings of Grzelak et al. [21] cannot be confirmed as they found a higher efficiency for larger porosity levels but were limited to small porosity levels.

Concerning the mean values, slight differences are apparent. The lowest porosity level of $\phi = 5.67\,\%$ has higher
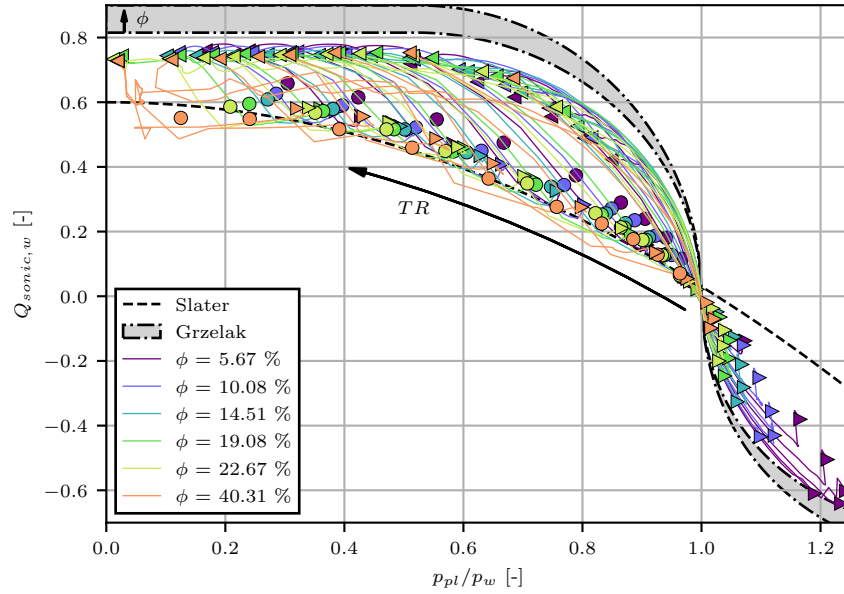
Fig. 26 Variation of the surface sonic flow coefficient for different porosity levels for the shock-boundary layer interaction

efficiency, and the highest level of $\phi = 40.31\%$ performs worse. For the rest, similar sonic flow coefficients are found with a higher pressure ratio for smaller porosity levels. However, high efficiency can not guarantee the control of the shock-boundary layer interaction.
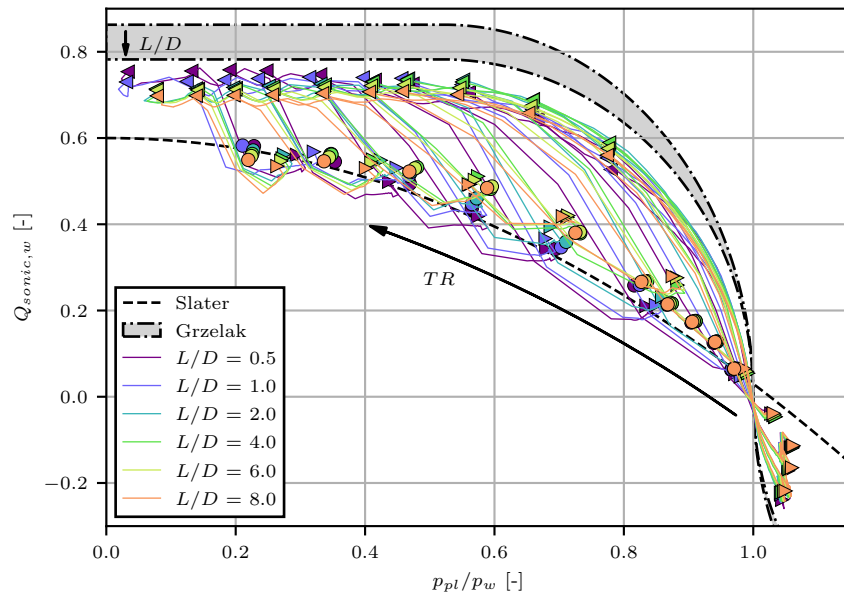

Fig. 27 Variation of the surface sonic flow coefficient for different length-to-diameter ratios for the shock-boundary layer interaction

C. Length-to-diameter ratio effects

As already stated in Sec. V.C, the length-to-diameter ratio has no significant effect on the boundary layer. Therefore, only the sonic flow coefficient is regarded in Fig. 27. Like for the other parameters, blowing occurs for small throat ratios. Here, small length-to-diameter ratios are slightly more efficient. As the tangential flow velocity inside the cavity is zero, and the pressure ratio is low, the flow inside the hole is fully attached, and hence the friction losses increase with the length of the holes.

The same length-to-diameter ratio effect is found for subsonic conditions and choked holes. The flow is already fully attached for low ratios, and the friction losses increase for higher length-to-diameter ratios. In contrast, for unchoked holes in subsonic conditions, the optimum length-to-diameter ratio is found for $L/D \approx 4$. Since the momentum close to the wall is not zero, a separated region inside the hole occurs. Thus, a particular hole length is necessary to enable flow reattachment. Grzelak et al. [21] found degradation of the bleeding performance for $L/D \geq 1.5$. However, no separated region is induced by external flow in their study, which explains the different findings.

VII. Conclusion and future work

This paper studied the influence of the hole diameter, the porosity level, and the length-to-diameter ratio on the performance of a porous bleed. The effect on the boundary layer thinning, the bleed mass flow rate and the shock-boundary layer interaction control were presented. For the final evaluation of the parameters, the differentiation between effectiveness and efficiency needs to be introduced. The effectiveness of the bleed describes the applicability to thin the boundary layer or control the shock no matter how much air has to be removed. On the contrary, the efficiency describes the evaluation of a porous plate on the surface sonic flow coefficient and the pressure ratio. Thus, a highly efficient plate can remove a high mass flow rate for a high pressure ratio p_{pl}/p_w.

The findings of the study prove the influence of the hole diameter on both effectiveness and efficiency. The smaller the hole diameter, the better the thinning of the boundary layer and the control of the shock-boundary layer interaction. Small hole areas correspond to smaller solid areas between the holes, which has a substantial impact on the effective control of the flow. Moreover, small holes are more efficient as they enable the removal of higher mass flow rates for equal pressure ratios.

The choice of the porosity level is, contrary to the hole diameter, a trade-off between effectiveness and efficiency. High-porosity plates guarantee the suction of sufficient mass flow rates to control the shock-boundary layer interaction and to thin the plate. However, high porosity levels correspond to an increased number of holes and thus to more pressure losses induced by the barrier shocks and expansion fans. As a result, low porosity levels are slightly more efficient.

The investigation of the length-to-diameter ratio confirms an impact on the bleed efficiency. As fully attached flow at the hole exit correlates with reduced pressure losses, a sufficient length of the hole needs to be ensured for an efficient application of the porous bleed. However, too long holes increase the friction losses and, as a result, the efficiency of the porous plate. Contrary to the other parameters, the length-to-diameter ratio does not affect the control of the shock-boundary layer interaction or the boundary layer thinning.

The present findings suggest several implications to existing porous bleed models, which do not consider the geometrical design of a porous plate. Further investigation of parameters such as the plate length or the plenum depth and width will need to be undertaken to explore other influences on bleed effectiveness and efficiency. Moreover, variation of the Mach number is required to examine the bleed behavior for subsonic conditions and to prove the general trend for supersonic conditions.

Acknowledgments

References

[1] Willis, B., Davis, D., and Hingst, W., "Flowfield measurements in a normal-hole-bled oblique shock-wave and turbulent boundary-layer interaction," *31st Jt. Propuls. Conf. Exhib.*, American Institute of Aeronautics and Astronautics, Reston, Viriginia, 1995. https://doi.org/10.2514/6.1995-2885.

[2] Willis, B., Davis, D., and Hingst, W., "Flow coefficient behavior for boundary layer bleed holes and slots," *33rd Aerosp. Sci.*

Meet. Exhib., American Institute of Aeronautics and Astronautics, Reston, Virigina, 1995. https://doi.org/10.2514/6.1995-31.

[3] Willis, B., and Davis, D., "Boundary layer development downstream of a bleed mass flow removal region," *32nd Jt. Propuls. Conf. Exhib.*, American Institute of Aeronautics and Astronautics, Reston, Virigina, 1996. https://doi.org/10.2514/6.1996-3278.

[4] Akatsuka, J., Watanabe, Y., Murakami, A., and Honami, S., "Porous Bleed Model for Boundary Condition of CFD Analysis," *3rd AIAA Flow Control Conf.*, American Institute of Aeronautics and Astronautics, Reston, Virigina, 2006. https://doi.org/10.2514/6.2006-3682.

[5] Oorebeek, J., Nolan, W., and Babinsky, H., "Comparison of Bleed and Micro-Vortex Generator Effects on Supersonic Boundary-Layers," *50th AIAA Aerosp. Sci. Meet. Incl. New Horizons Forum Aerosp. Expo.*, American Institute of Aeronautics and Astronautics, Reston, Virigina, 2012. https://doi.org/10.2514/6.2012-45.

[6] Oorebeek, J., and Babinsky, H., "Flow physics of a normal-hole bled supersonic turbulent boundary layer," *51st AIAA Aerosp. Sci. Meet. Incl. New Horizons Forum Aerosp. Expo.*, American Institute of Aeronautics and Astronautics, Reston, Virigina, 2013. https://doi.org/10.2514/6.2013-526.

[7] Oorebeek, J., Babinsky, H., Ugolotti, M., Orkwis, P. D., and Duncan, S., "Experimental and Computational Investigations of a Normal-Hole-Bled Supersonic Boundary Layer," *AIAA J.*, Vol. 53, No. 12, 2015, pp. 3726–3736. https://doi.org/10.2514/1. J053956.

[8] Bodner, J., Greber, I., Davis, D., and Hingst, W., "Experimental investigation of the effect of a single bleed hole on a supersonic turbulent boundary-layer," *32nd Jt. Propuls. Conf. Exhib.*, American Institute of Aeronautics and Astronautics, Reston, Virigina, 1996. https://doi.org/10.2514/6.1996-2797.

[9] Davis, D., Vyas, M., and Slater, J., "Research on Supersonic Inlet Bleed," *50th AIAA Aerosp. Sci. Meet. Incl. New Horizons Forum Aerosp. Expo.*, American Institute of Aeronautics and Astronautics, Reston, Virigina, 2012. https://doi.org/10.2514/6.2012-272.

[10] Eichorn, M., Barnhart, P., Davis, D. O., Vyas, M., and Slater, J., "Effect of Boundary-Layer Bleed Hole Inclination Angle and Scaling on Flow Coefficient Behavior," *51st AIAA Aerosp. Sci. Meet. Incl. New Horizons Forum Aerosp. Expo.*, American Institute of Aeronautics and Astronautics, Reston, Virigina, 2013. https://doi.org/10.2514/6.2013-424.

[11] Hingst, W., and Tanji, F., "Experimental investigation of a two-dimensional shock-turbulent boundary layer interaction with bleed," *21st Aerosp. Sci. Meet.*, American Institute of Aeronautics and Astronautics, Reno, Nevada, 1983. https: //doi.org/10.2514/6.1983-135.

[12] Benhachmi, D., Greber, I., and Hingst, W., "Experimental and numerical investigation of an oblique shock wave/turbulent boundary layer interaction with continuous suction," *27th Aerosp. Sci. Meet.*, American Institute of Aeronautics and Astronautics, Reston, Virigina, 1989. https://doi.org/10.2514/6.1989-357.

[13] Davis, D. O., Willis, B., and Schoenenberger, M., "Porous and microporous honeycomb composites as potential boundary-layer bleed materials," *33rd Jt. Propuls. Conf. Exhib.*, American Institute of Aeronautics and Astronautics, Reston, Virigina, 1997. https://doi.org/10.2514/6.1997-3260.

[14] Slater, J. W., "Improvements in Modeling 90-degree Bleed Holes for Supersonic Inlets," *J. Propuls. Power*, Vol. 28, No. 4, 2012, pp. 773–781. https://doi.org/10.2514/1.B34333.

[15] Shih, T. I., and Teh, E.-J., "Reynolds-Averaged Simulations of Shock-Wave/Boundary-Layer Interactions with Bleed," *51st AIAA Aerosp. Sci. Meet. Incl. New Horizons Forum Aerosp. Expo.*, American Institute of Aeronautics and Astronautics, Reston, Virigina, 2013. https://doi.org/10.2514/6.2013-423.

[16] Choe, Y., Kim, K., Kim, J., and Kim, C., "Supersonic Inlet Design using Bleed Boundary Condition with Porosity Variation and Expansion Wave," *2018 AIAA Aerosp. Sci. Meet.*, American Institute of Aeronautics and Astronautics, Reston, Virginia, 2018. https://doi.org/10.2514/6.2018-0540.

[17] Zhang, B.-h., Zhao, Y.-x., and Liu, J., "Effects of bleed hole size on supersonic boundary layer bleed mass flow rate," *J. Zhejiang Univ. A*, Vol. 21, No. 8, 2020, pp. 652–662. https://doi.org/10.1631/jzus.A1900507.

[18] Akar, G., and Eyi, S., "Computational Modelling and Analysis of Porous Bleed Holes at Supersonic Speeds," *AIAA Propuls. Energy 2020 Forum*, American Institute of Aeronautics and Astronautics, Reston, Virginia, 2020. https://doi.org/10.2514/6.2020-3721.

[19] Doerffer, P. P., and Bohning, R., "Modelling of perforated plate aerodynamics performance," *Aerosp. Sci. Technol.*, Vol. 4, No. 8, 2000, pp. 525–534. https://doi.org/10.1016/S1270-9638(00)01063-4.

[20] Harloff, G. J., and Smith, G. E., "Supersonic-inlet boundary-layer bleed flow," *AIAA J.*, Vol. 34, No. 4, 1996, pp. 778–785. https://doi.org/10.2514/3.13140.

[21] Grzelak, J., Doerffer, P., and Lewandowski, T., "The efficiency of transpiration flow through perforated plate," *Aerosp. Sci. Technol.*, Vol. 110, 2021. https://doi.org/10.1016/j.ast.2021.106494.

[22] Benoit, C., Péron, S., and Landier, S., "Cassiopee: A CFD pre- and post-processing tool," *Aerosp. Sci. Technol.*, Vol. 45, 2015, pp. 272–283. https://doi.org/10.1016/j.ast.2015.05.023.

[23] Cambier, L., Heib, S., and Plot, S., "The Onera elsA CFD software: input from research and feedback from industry," *Mech. Ind.*, Vol. 14, No. 3, 2013, pp. 159–174. https://doi.org/10.1051/meca/2013056.

[24] Spalart, P., "Strategies for turbulence modelling and simulations," *Int. J. Heat Fluid Flow*, Vol. 21, No. 3, 2000, pp. 252–263. https://doi.org/10.1016/S0142-727X(00)00007-2.